Temporal reformatting of odor signals by flow environments

Elle Stark,[1] Aaron True,[1] John P. Crimaldi,[1,*] and Jonathan D. Victor[2]

[1] *University of Colorado Boulder, Department of Civil, Environmental, and Architectural Engineering, Boulder, CO, USA*

[2] *Weill Cornell Medicine, Brain and Mind Research Institute, Division of Systems Neurology and Neuroscience, New York, NY, USA*

In broad terms, the goal of a sensory system is to allow an organism to gain information about the external world, taking into account the physical processes that intervene between the sources of the signals and the organism's receptors. In olfaction, these transformations may be particularly complex, as they include the fluid mechanics of odorant transport, which is often turbulent. Here, we focus on this transformation, viewing it as an inescapable signal processing stage that occurs before sensory transduction. The typically passive nature of an odorant (i.e., that it is carried by the flow, but does not affect the flow) allows for a concise characterization of how flow transforms the temporal characteristics of odorant concentration at the source into its temporal characteristics downstream. Specifically, the power spectrum (but not the odor concentration time series itself) is transformed in a linear fashion: spectral components at the source are filtered and mapped to other frequencies at a downstream sensor. We characterize the dominant processes in the mapping as 1) frequency filtering acting as a low-pass filter on the source signal, 2) frequency spreading that redistributes power about the source frequency, and 3) frequency production of an underlying spectrum regardless of input frequency. Each of these processes arises naturally from the multiscale nature of turbulent flow environments. This machinery provides a framework for comparison with active sensation, viewed as another form of signal processing that occurs prior to sensory transduction.

I. INTRODUCTION

Odor signals drive crucial animal behaviors, yet olfaction presents a unique challenge among sensing modalities due in large part to the transformations of the signal that occur between release at the source, transport through a fluid flow medium, interaction with animal sensing architecture, and reception and encoding by the animal [1–5]. It is increasingly appreciated that olfaction is a *fast* sense: the transduction process is rapid [6, 7], and rapid fluctuations in odorant concentration can support behavioral decisions [8, 9]. This prioritizes the need to understand the temporal dynamics of odorants in natural environments, and thus, on the physics of turbulence. The main goal of this paper is to connect the physics of transport by turbulent flows to a formalism that concisely characterizes how flows transform the dynamics of olfactory signals, viewed in the frequency domain as a signal-processing transformation between source and receptor. Improving our understanding of these transformations provides value for both understanding signal properties in naturalistic odor plumes [10] and for generating and quantifying odor stimuli in laboratory experiments [11].

The spectral content of a signal plays an important role in olfactory navigation, in tasks ranging from detection of the odor [12] to discrimination between different odorants [13] to extracting information and driving behavioral decisions during navigation [8]. Though olfaction was historically considered a slow sense, recent studies demonstrate the availability of fast signal dynamics to navigating organisms, including the ability to discriminate odor signals up to 40 Hz in mice [14], and up to 1000 Hz in insects [6]. At the mechanistic level, olfactory receptor neurons show more sensitivity to fluctuating signals than static signals [15, 16]; the fluctuations in odor signal produced by turbulent transport may therefore benefit the task of detection. For discrimination tasks, minute differences in the temporal kinetics between different odorants provides a key mechanism for identification of distinct odors in the presence of multi-component mixtures and various background odors [13, 17]. During navigation, animals also show behavioral responses to fast dynamics in odor signals [18], and leverage temporal characteristics such as the intermittency of odor encounters [9, 19] and the motion of odor filaments [20] for navigational decisions.

To characterize the changes to the spectral content of odor signals during turbulent transport, we turn to fluid dynamics approaches. A rich physics tradition investigates transport of scalar materials by turbulent flow fields, providing a robust foundation for considering odor signal transformations by the fluid flow. Using a fluid dynamics perspective, we note that odors typically behave as *passive scalars*: the odor does not influence the flow dynamics that carries it away from the source [21, 22]. As a parcel of odor moves downstream, turbulent eddies stretch it into filaments that fold, spread, rotate, and mix with the surrounding medium, continuously generating high-frequency patterns in the odor signal; meanwhile, molecular diffusion works to smooth out gradients in the odor concentration, dampening the amplitude of low-frequency signals and quickly erasing high-frequency signals [23]. In fluid dynamics literature, these processes have been framed in terms of the turbulent production,

* Contact author: crimaldi@colorado.edu

transport and dissipation of variance in the transported scalar. The odor signal that reaches an organism represents a combination of these interacting processes, generating a complex and dynamic signal that varies with respect to both space and time [24]. Research as early as the 1930s has employed frequency-based spectral analyses to describe and investigate these turbulent transport processes [25, 26], as reviewed in [27].

At the intersection of olfaction and turbulent transport physics, there is a small body of literature that specifically considers statistical and spectral properties of turbulent plumes in the context of olfactory sensing and navigation. Specifically, [28] demonstrated the utility of Lagrangian approaches (that is, those that involve tracking packets of odor using a moving frame of reference) for characterizing the statistics of odor signals emitted from a given source at a continuous rate. They employ backward-time Lagrangian tracking of odor packets to develop time-domain probability distributions for the intensity, duration, and spacing in time of odor detection events, or "whiffs", at various distances downstream. The methods herein also employ Lagrangian analysis strategies, but with the goal of frequency-domain descriptions of how odor signals transform after emission from sources that may contain a broad range of frequency content. Other olfaction literature has leveraged frequency domain analysis (but not Lagrangian approaches) to interrogate specific aspects of odor plume dynamics, including investigations of separation distance between multiple sources [29] and experimental measurement of the spectral content of flow and chemical signals in aqueous plumes[30, 31]. Such frequency domain descriptors provide a direct connection to sensory processing analysis, which is often characterized in the frequency domain not only for olfaction, but other senses as well [32–35].

The Lagrangian-based, frequency domain analysis herein characterizes the transformation of odor signals in terms of how the power spectrum is changed from source to sensor. As we show, even for complex flows, the power spectrum at the sensor is a linear transformation of the power spectrum at the source. This transformation typically includes filtering of spectral components as well as mapping components from one frequency to another. Such a framing of transport as a filter on the odor signal echoes literature in olfactory neuroscience that models olfactory reception as quasilinear processes. For example, [36] characterizes first-order olfactory neuron responses in terms of a low-pass transduction filter and a uniform high-pass filter for spike generation, and [37] utilizes a Linear-Nonlinear-Poisson computational model for olfactory neuron responses.

While our specific analysis considers passive odor transport in airborne plumes far from any boundaries, the framework presented is applicable across many navigational contexts. More precisely, the framework presented here holds so long as the transport process remains linear with respect to the odor concentration, which stays true across many olfactory landscapes. Exceptions are scenarios in which the odor itself affects the flow field dynamics, or in which the odor interacts with surfaces that exhibit nonlinear sorption processes. We further explore the generalizability and limits of this framework in the discussion.

As will be shown, the framework reveals that the spectral transformations to the odor signal exhibit three key dynamic processes, which we refer to as frequency filtering, frequency spreading, and frequency production. For clarity, we first introduce each of these three processes in isolation through idealized cases that show how a single one of these processes affects the frequency content of a sensory signal. We then apply the approach to a more complex scenario, using computational fluid dynamics to simulate a two-dimensional chaotic flow that transports a fluctuating odor signal. We show how a combination of the three key dynamic processes are responsible for the primary mapping characteristics observed in the complex case, with evidence from the results as well as connections to fluid dynamics literature. By characterizing the effects of turbulent transport as a signal-processing step, the temporal reformatting due to flows is expressed in terms that are directly meaningful in terms of sensory processes. The results can then be situated within a larger framework of frequency transformations that occur from odor signal emission, across turbulent transport, then active sensation by an animal, to reception, neural response, and finally behavioral decisions in olfactory search.

II. RESULTS

Through a paired-particle analysis of odor transport in a chaotic flow field, we identified three dominant processes in the reformatting of an odor signal by a turbulent flow: frequency *filtering*, frequency *spreading*, and frequency *production*. Frequency filtering refers to a frequency-by-frequency attenuation of power in higher frequencies in the flow. Transport processes act as a low-pass linear filter on the odor signal, driven by particle dispersion. Frequency spreading refers to the redistribution of power across a wider range of frequencies centered on each original frequency in the odor signal, driven by multi-scale interactions in the flow, which can be described by the turbulent energy cascade. Frequency production refers to the imparting of a new spectrum onto the odor signal, whose characteristics are independent of frequencies present in the original signal. The power spectrum in the flow field, which then induces a characteristic spectrum onto transported material in the flow, drives the frequency production component.

In this section, we describe the analysis and illustrate each of these components with an idealized case that isolates it. We then show results for an example turbulent transport of a fluctuating odor in a naturalistic flow, demonstrating the presence of all three components in the signal reformatting results. Finally, we vary key pa-

rameters of this example to evaluate their impacts on reformatting. Throughout this section, we illustrate the mapping function using three-dimensional plots; to orient the reader, we recommend viewing the plot rotation animations provided in the supplementary materials [38].

A. Analysis

To analyze odor plumes from a signal processing perspective, we consider a system consisting of a point source emitting an odor signal at a given location, a finite-sized sensor at some distance downstream of the source that receives the signal, and a flow field that transports the odor from the source to the sensor (Fig. 1). The source signal may contain a range of frequencies; for instance, a female moth may release pheromone pulses at various intervals [39]. Transport through the flow field can then be characterized as a mapping function that transforms the power spectrum of the source signal, $\tilde{P}_{\text{source}}$, into the power spectrum of the signal received by the sensor downstream, $\tilde{P}_{\text{sensor}}$. (Here and throughout the manuscript, a tilde denotes a frequency-domain quantity.)

To compute the frequency mapping from source to sensor, we use a Lagrangian particle-tracking approach, in which small packets of odor, which we refer to herein as "particles", are emitted from a point source located at the origin. We describe the approach intuitively here; mathematical details are provided in Appendix B.

First, consider a single particle that travels from the source to some downstream sensor at a fixed location, whose trajectory has an associated travel time. If many different particles are released over time from the source, travel times will vary depending on the particular flow field realization at that time along with random motion from molecular diffusion. By tracking many particle trajectories, we can build up a probability distribution of particle travel times from the source to a given sensor location (a distribution that depends on the sensor distance from the source).

Next, to analyze the effects on the power spectrum, we need to consider pairs of particles. This is because the power spectrum is the Fourier transform of the autocovariance, i.e., the covariance between fluctuations in odor concentration at pairs of times. Just as the distribution of odor concentrations can be built up by tracking single particles, the joint distribution at pairs of times can be built up by tracking two particles as a pair. The two particles in the pair differ in release times, which is affected by the frequency content of the source, and their arrival times to the sensor, which relates to the frequency content at the sensor. The difference in arrival times depends both on the difference in release times and the difference in travel times, which in turn depends on the particulars of the flow field. We thus characterize the paired particle behavior in terms of the likelihood that two particles have some difference between their travel times, given a difference in release times. These statistics are then converted to the frequency domain via Fourier Transforms to yield a compact signal processing description of the transformation on the odor signal spectrum from source to sensor.

Importantly, viewed as an operation on power spectra, the odor signal transformation from source to sensor is linear. The reason for this, in essence, is that the power spectrum is the Fourier transform of the autocorrelation function, and the autocorrelation function depends only on the pairwise statistics of the odor particles (computed as described above). The pairwise statistics at the sensor are determined by the pairwise statistics at the source, along with a characterization of the joint probability of their arrival times. We assume that this characterization is known, and we show in Appendix B that it yields a frequency-domain transformation

$$\tilde{P}_{\text{sensor}}(\omega) = \frac{1}{2\pi} \int_{-\infty}^{\infty} \tilde{P}_{\text{source}}(\omega+\lambda)\tilde{B}(\omega,\lambda)\,\mathrm{d}\lambda, \qquad (1)$$

where the mapping function $\tilde{B}(\omega,\lambda)$ depends on the flow field and describes how the frequency spectrum is transformed between the source and the sensor. In some simple idealized cases $\tilde{B}$ can be determined analytically, while in more complex cases, such as those in naturalistic turbulent flows, a data-driven approach is required.

In the subsections below, we examine scenarios that each isolate one of these components: frequency filtering, driven by particle dispersion in the flow, frequency spreading, driven by the energy cascade across scales in turbulence, and frequency production, driven by the energy cascade imparting a characteristic spectrum onto any transported material. In each case, we begin with an intuitive view and then take a more quantitative approach. We then analyze a more complex turbulent transport scenario that combines these components. We parse naturalistic turbulent transport into the three behaviors with a characterization that draws directly from fluid dynamics literature regarding primary processes in the dynamics of turbulent flow and transport, as further explored in Sec. III B.

B. Idealized case 1: frequency filtering

Molecular diffusion in uniform laminar flow isolates and illustrates frequency filtering behavior. Molecular diffusion results from Brownian motion of molecules, which move independently of one another (using a reference frame that travels with the uniform flow). Because of this independence, the arrival time statistics of two particles are independent of the release interval. In the frequency domain, this independence translates into a function $\tilde{B}(\omega,\lambda)$ that is concentrated at λ=0. Moreover, because the particles move independently, the joint distribution of their travel times is the product of the distribution of a single particle's travel time, $a(t)$. As shown

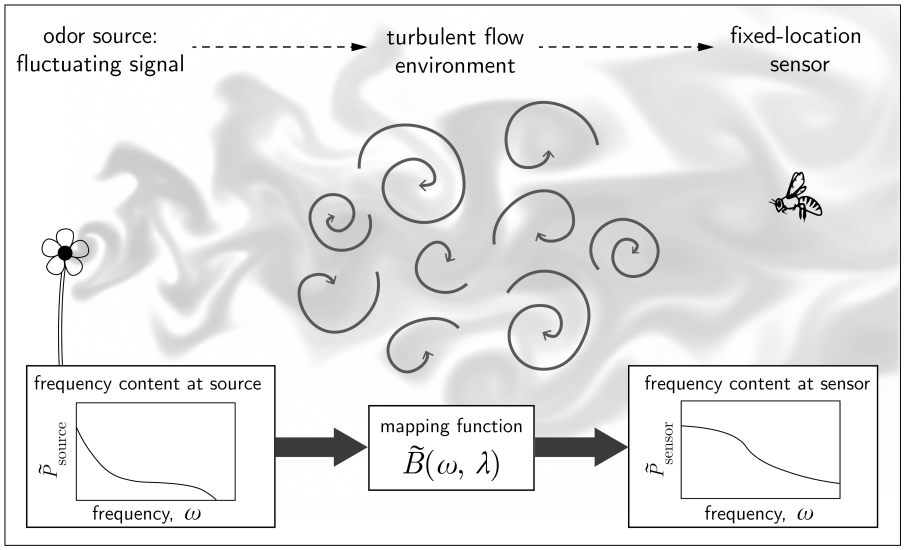

FIG. 1. Conceptual overview of the system of interest, depicting a fluctuating source signal whose power spectrum, $\tilde{P}_{\text{source}}$, is transformed by turbulent transport into a new spectrum at the sensor, $\tilde{P}_{\text{sensor}}$. The transformation is characterized by a mapping function, $\tilde{B}(\omega, \lambda)$, that depends on both the source frequency, ω, and a term related to the autocorrelation of the velocity field, λ.

in Appendix B, this leads to a mapping function $\tilde{B}(\omega, \lambda)$ given by $2\pi\delta(\lambda)|\tilde{a}(\omega)|^2$. The ω-dependence of the mapping function $\tilde{B}(\omega, \lambda)$, $|\tilde{a}(\omega)|^2$, is the Fourier transform of the autocovariance of the distribution $a(t)$ of travel time for a single particle to reach the sensor.

Thus, in this case, eq. 1 reduces to

$$\tilde{P}_{\text{sensor}}(\omega) = \tilde{P}_{\text{source}}(\omega)|\tilde{a}(\omega)|^2, \tag{2}$$

where $\tilde{a}(\omega)$ is the Fourier transform of the distribution of travel times for a single particle. Therefore, the transformation from the source power spectrum to the sensor power spectrum is that of a linear filter.

Next, we can estimate the filter's behavior using known physics of molecular diffusion. Concretely, we quantify the filter's impulse response by leveraging the solution to the one-dimensional advection-diffusion equation:

$$C(x,t) = \frac{1}{\sqrt{4\pi D t}} \exp\left(-\frac{(x-\overline{u}t)^2}{4Dt}\right) \tag{3}$$

where $C(x,t)$ is the odor's concentration at a given time t and streamwise coordinate x (in other words, x represents the centerline distance downstream of the source), D is the molecular diffusion coefficient of the odor, and the mean location is $\overline{u}t$, where $\overline{u}$ is the average flow velocity. Leveraging this solution in our problem setup, which has fixed sensor locations, requires converting from a distribution in space for a given point in time into a distribution in time for a given point in space. Here, we employ a convenient Gaussian approximation by assuming that the diffusivity is small relative to advection and induces minimal changes to the distribution during the time it takes to advect past a point in space. We can then set $t = x/\overline{u}$ and represent $a(t)$, the distribution of travel times for a single particle, as a Gaussian in time:

$$C(x,t) \approx \frac{1}{\sqrt{4\pi D x/\overline{u}^3}} \exp\left(-\frac{(t-x/\overline{u})^2}{4Dx/\overline{u}^3}\right) \tag{4}$$

We set the mean to zero then take the Fourier transform to convert from the impulse response to the filter's frequency response, $\tilde{a}(\omega)$:

$$\tilde{C}(\omega, x) \approx \exp\left[\frac{-\omega^2 D x}{\overline{u}^3}\right] \tag{5}$$

Substituting this estimate of $\tilde{a}(\omega)$ into eq. 2, we arrive at a Gaussian approximation of the mapping of power in a laminar diffusion case:

$$\tilde{P}_{\text{sensor}}(\omega) \approx \tilde{P}_{\text{source}}(\omega) \exp\left[\frac{-2\omega^2 D x}{\overline{u}^3}\right]. \tag{6}$$

We will use this Gaussian approximation in the filtering component for our naturalistic case; here, Fig. 2A illustrates a numerically computed solution for this transformation and its dependence on distance from the source. The power at each input frequency is mapped to the same output frequency, resulting in the knife-edge on the diagonal. In the characteristic manner of a filter with a Gaussian frequency response, high frequencies are attenuated, and this attenuation becomes more severe with increasing distance from the source due to increased travel time and associated increased diffusion.

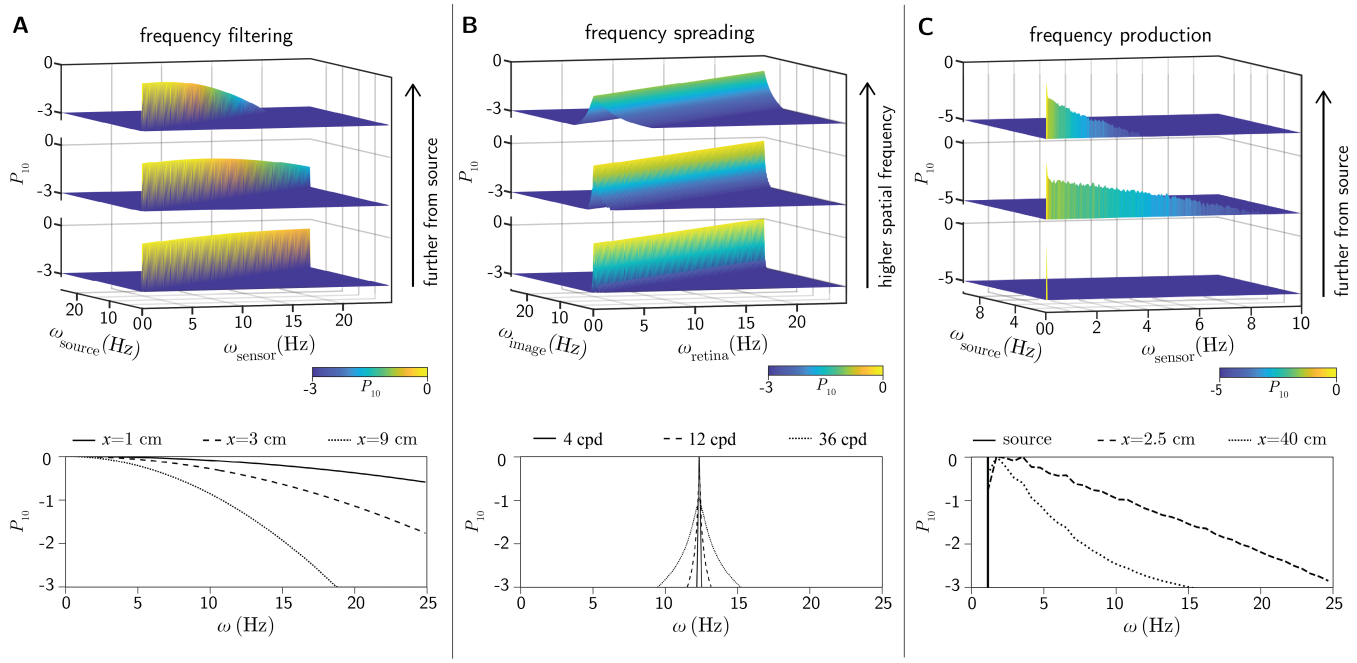

FIG. 2. Idealized cases illustrating three key processes in the turbulent transport of an odor signal, where P_{10} represents the log of the power spectral density for each frequency. (A) Diffusion with ideal laminar flow, with a diffusion constant of 0.012 cm^2/s, flow velocity 6 cm/s, and sensor distance (bottom to top) of 1, 3, and 9 cm. Below, transects along the diagonal from (0, 0) to (25, 25) for the three locations. (B) Transformations due to fixational eye movements, with a diffusion constant of 0.006 deg^2/s and spatial frequencies (bottom to top) of 4, 12, and 36 cycles/deg. Below,transects along the diagonal from (0, 25) to (25, 0) for the three spatial frequencies. (C) Results of the damped-source case that enters the flow with frequency spectrum concentrated at 0 Hz, with diffusivity 1.5×10^{-5} m^2/s, and sensor distance (bottom to top) of 0, 2.5, and 40 cm. Below, transects at 0 Hz source frequency for the three locations.

C. Idealized case 2: frequency spreading

A second dynamic process in odor transport spreads the power at each source frequency into a wider range of frequencies present at the sensor. Frequency spreading is a convolution in the frequency domain, so it corresponds to a multiplicative process in the time domain. More formally, frequency spreading is described by

$$\tilde{P}_{\text{sensor}}(\omega) = \frac{1}{2\pi} \int_{-\infty}^{\infty} \tilde{P}_{\text{source}}(\omega + \lambda)\tilde{q}(\lambda)\, \mathrm{d}\lambda, \qquad (7)$$

a limiting case of eq. 1 in which $\tilde{B}(\omega, \lambda) = \tilde{q}(\lambda)$ has no dependence on ω. As shown in the Appendix, $\tilde{q}(\lambda)$ is the Fourier transform of $q(t)$, the probability that two particles emitted with a temporal separation t are both absorbed. This sampling process is the multiplication mentioned above, and its statistics determine the frequency spreading.

Frequency spreading in pure form, i.e., in which the extent of spreading is independent of source frequency, only occurs when there is no temporal dispersion (though a fixed transport delay may be present). In principle, an idealized sampling process, e.g., an antenna that moves into and out of a plume, could manifest this behavior, provided that there is no temporal dispersion in the flow itself.

The absence of temporal dispersion is unrealistic in a flow. In contrast, sampling without temporal dispersion does occur in another biologically-important active-sensing context: vision, where it indeed yields the frequency-spreading phenomenon in isolation.

In this scenario, sampling is a result of fixational eye movements (FEMs). FEMs occur in the periods *between* saccades — the well-known shifts of gaze that occur several times per second. As such, FEMs transform a largely static visual image into a moving pattern on the retina [40], a spatiotemporal remapping that is essential to normal vision[41]. FEMs enable a single photoreceptor to sample the projected image. As the only transport delay is photon travel time, there is no temporal dispersion. Moreover, although there is good evidence that FEMs are under neural control [42], their statistics are well-approximated by that of Brownian motion[40].

Another characteristic of vision helps to illustrate a second aspect of the frequency-spreading process. In vision, the spatial structure of the stimulus (e.g., shape, texture) is critical. Importantly, the sampling process, for any given eye movement path, is a linear function of the image itself. (That is, the signal generated by sampling a superposition of images is the superposition

of the signals generated by sampling each image separately). Thus, as is standard in the analysis of linear systems, the effects of sampling can be analyzed by considering each spatial Fourier component separately, i.e., at each spatial frequency. We therefore consider the visual image to consist of a sinusoid of spatial frequency $\vec{k}$. The joint probability that two "particles", emitted with an interval τ, both arrive at the sensor corresponds to the expected value of the product of the intensity of two points on the sinusoid: one at a reference position, and one after Brownian motion of the eye for a time τ. For a diffusion constant D, this is given by

$$q(\tau, \vec{k}) = \exp\left(-\frac{D\,|\tau|\,\left|\vec{k}\right|^2}{2}\right). \tag{8}$$

The (temporal) Fourier transform of $q(\tau, k)$ (see also the Supplement of [41]) is given by

$$\tilde{q}(\lambda, \vec{k}) = \frac{\left|\vec{k}\right|^2 D}{\left|\vec{k}\right|^4 \frac{D^2}{4} + \lambda^2}. \tag{9}$$

The resulting transformation is illustrated in Fig. 2B for a range of spatial frequency magnitudes $|\vec{k}|$. In each case, the power spectrum at the sensor is a convolution of the power spectrum at the source, with a kernel (eq. 9) that widens as spatial frequency increases. In vision, an increase in spatial frequency can be produced by a larger viewing distance, or, by decreasing the spatial scale of the object itself; both of these lead to greater frequency spreading. In idealized olfactory sampling, frequency spreading also increases when the effective "spatial frequency" of the odor increases. Since the sensor is always in contact with the odorant, an increase in spatial frequency corresponds to a decreasing spatial scale of the concentration variations in the plume.

D. Idealized case 3: frequency production

For the frequency production component, we consider the case of an odor signal whose fluctuations are instantaneously damped upon release, prior to entering the flow. This case essentially represents an odor that is released at a constant rate into a turbulent flow field, so the only frequency component in the odor signal that persists into the flow field is 0 Hz. When a continuous odor signal is released into a turbulent flow field, new frequencies are introduced by the fluctuations in the flow velocity as the odor travels downstream. The introduction of such fluctuations to the signal may benefit animal olfactory navigation in several ways. Firstly, it likely benefits detection tasks, as the sensory system is more sensitive to fluctuating signals than static odors [15, 16]. Second, it may benefit source localization tasks if we consider some specifics of the odor spectrum characteristics. Near to the source, the odor signal retains information about the source configuration (its size, position relative to boundaries, etc.) [43], but far from the source, the odor signal "forgets" the source configuration and instead is primarily dependent on the flow characteristics. Thus, the presence - or absence - of a signature of the source characterization within the spectrum of an odor signal may also provide a navigating animal with information about its position relative to the source.

In terms of our mathematical framework, because the power spectrum of an unvarying continuous source is concentrated at 0 Hz, i.e., $\tilde{P}_{\text{source}}(\omega) = 2\pi\delta(\omega)\tilde{P}_0$, eq. 1 reduces to

$$\tilde{P}_{\text{sensor}}(\omega) = \tilde{P}_0 \tilde{B}(\omega, -\omega). \tag{10}$$

The dynamics of turbulent flows determine the form of $\tilde{B}(\omega, -\omega)$. Turbulent flows exhibit fluctuations in their velocity fields, which then impart fluctuations to the initially constant odor signal. These fluctuations produce a broad range of frequencies in the signal, reflecting the broad range of length and time scales present in the flow (this idea can be thought of as a range of differently sized eddies existing at any given time throughout the flow field). The resulting spectrum of the transported odor exhibits a characteristic behavior with a power scaling regime and a diffusive cutoff regime, as described in the seminal work of Batchelor [44]. This behavior allows us to express the power $\tilde{P}_{\text{sensor}}(\omega)$ at a given frequency ω as:

$$\tilde{P}_{\text{sensor}}(\omega) = A\omega^{-\alpha} \exp\left(-\gamma\omega^2\right) \tag{11}$$

where A is a constant, α is an effective power law exponent, and γ is a diffusive cutoff factor.

To provide a specific example, we introduce the 2-dimensional simulated chaotic flow field that we will further investigate in the naturalistic odor transport case below. As shown in Fig. 3, the computational fluid dynamics model consists of a uniform flow (at speed 0.1 m/s) passing across a mixing grid cylinder array to induce a chaotic flow field, whose turbulent kinetic energy decays streamwise across a 0.75 × 0.6 m domain. The computational model directly solves the Navier-Stokes and continuity equations to produce the velocity field. For this idealized case study, we also directly solve for the odor concentration field using the advection-diffusion equation to transport odor from the initially constant-concentration source. The 180-second simulation provides 50 Hz data at 500 μm resolution, providing statistically sufficient and well-resolved data to serve as an analysis testbed for a naturalistic plume (see Appendix C for additional model details and testing).

With this computational model, we characterize the frequency-generation process by Fourier analysis of the concentration time series in the simulated odor plume at several point locations relative to the source. Fig. 2C shows the resulting spectra. As illustrated, the odor signal is transformed from a steady signal into one whose

spectrum contains a wide range of frequencies, and that evolves as the velocity field spectrum evolves over the domain. This idealized case demonstrates the third primary reformatting process: frequency production.

E. Naturalistic case: fluctuating odor source in turbulent flow

Next we quantify the case of an odor source emitting a signal with more complex frequency content (i.e., a fluctuating source signal), which is then transported via the turbulent flow to a downstream sensor. The resulting transformation imparted onto the odor signal includes contributions from all three processes described above.

To carry out the particle tracking analysis, we first obtained velocity data using the same two-dimensional computational fluid dynamics model described above to generate the evolving chaotic flow field, shown in Fig. 3. The source for particles is set at (0,0) and a small, finite area downstream of the source represents the sensor. We tested seven sensor locations, each with 0.02 m streamwise thickness and with cross-stream widths that expand as $\sqrt{Dt}$ to take into account plume expansion, as illustrated in Fig. 3 (thus ensuring sufficient particles pass through the sensor area downstream; effects of sensor size are explored in Sec. II F). The sensor does not affect the particle trajectories; a particle is 'sensed' simply when its trajectory carries it through the specified area of the sensor.

Particle trajectories are computed by numerical advection by the velocity field and molecular diffusion via Brownian motion (implemented as a random Wiener process). The massless tracer particles are released at $\mathbf{x}$ =(0,0) and numerically transported to position $\mathbf{x}(t)$ by

$$\mathbf{x}_{t+\Delta t} = \mathbf{x}_t + \mathbf{u_t}\Delta t + \mathbf{Z}\sqrt{2D\Delta t}, \tag{12}$$

where $\mathbf{u}_t$ is the velocity field, D is molecular diffusivity of the odor, and $\mathbf{Z}$ is a Gaussian process with mean 0 and variance 1. We next use the travel time data to determine the mapping function $\tilde{B}(\omega, \lambda)$ (See Appendix B for details). First, we define $b(\tau_1, \tau_2, \tau_{21})$ as the joint probability of particles with travel times τ_1 and τ_2 arriving at the sensor, given that their release times differ by τ_{21} (positive if particle 2 is released after particle 1). Then, we compute its Fourier transform,

$$\tilde{b}(\omega_1, \omega_2, \lambda) = \int_{-\infty}^{\infty}\int_{-\infty}^{\infty}\int_{-\infty}^{\infty} b(\tau_1, \tau_2, \tau_{21}) \cdot e^{-i\omega_1\tau_1 - i\omega_2\tau_2 - i\lambda\tau_{21}} d\tau_1 d\tau_2 d\tau_{21}. \tag{13}$$

The mapping function is now given by

$$\tilde{B}(\omega, \lambda) = \tilde{b}(\omega, -\omega, \lambda). \tag{14}$$

For fluctuating odors transported in our simulated chaotic flow field, the paired particle analysis reveals frequency mappings that follow the trends shown in Fig. 4. As illustrated, the frequency mapping for the turbulent transport case involves all three primary components observed in the simplified cases: filtering, spreading, and production. In the following sections, we investigate the dynamic processes driving each component. First, we quantify the linear frequency filtering using an effective diffusion model of turbulent transport. Next, we compute the spectrum of the flow field to illustrate the multi-scale nature of the turbulent flow that spreads power across a wider range of frequencies. Third, we use the energy cascade to explain the underlying power spectrum imparted to the signal due to frequency production in the transport process. Finally, we explore how the results depend on relevant physical parameters.

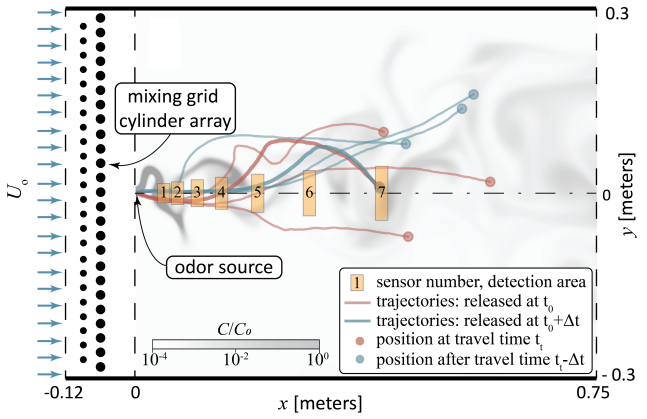

FIG. 3. Schematic of the computational fluid dynamics model used for generating the velocity field for the paired-particle analysis, along with the concentration field for the idealized frequency production case. Uniform inlet flow U_0 is passed over a cylinder array whose interacting cylinder wakes generate turbulent kinetic energy, which decays across the 0.75 m domain. The gray shading shows an example snapshot of a concentration field modeled for an odor source located at the origin, to provide a sense of the plume extent and the coherent structures present in the velocity field. Example particle trajectories are plotted for two different release times - the red particles at t_0 and the blue particles at $t_0 + \Delta t$. Note that while particles released at the same time tend to be more correlated than particles released at different times, even particles released at the same time can become separated due to diffusion. Gold boxes represent the seven sensor bounds, each with streamwise thickness 0.02 m, at x-distances (x_i) of 0.05, $0.05\sqrt{2}$, 0.1, $0.1\sqrt{2}$, 0.2, $0.2\sqrt{2}$, and 0.4 m downstream of the source, and with the following cross-stream widths that expand as $\sqrt{x_i/x_0}$ (to take plume expansion into account): 0.031, 0.037, 0.044, 0.052, 0.062, 0.073, and 0.087 m.

Process 1: particle dispersion filters high frequencies

To investigate the frequency filtering process in naturalistic flows, we begin by developing a mathematical model for the linear filtering of input frequencies, analogous to the behavior of the laminar diffusion case.

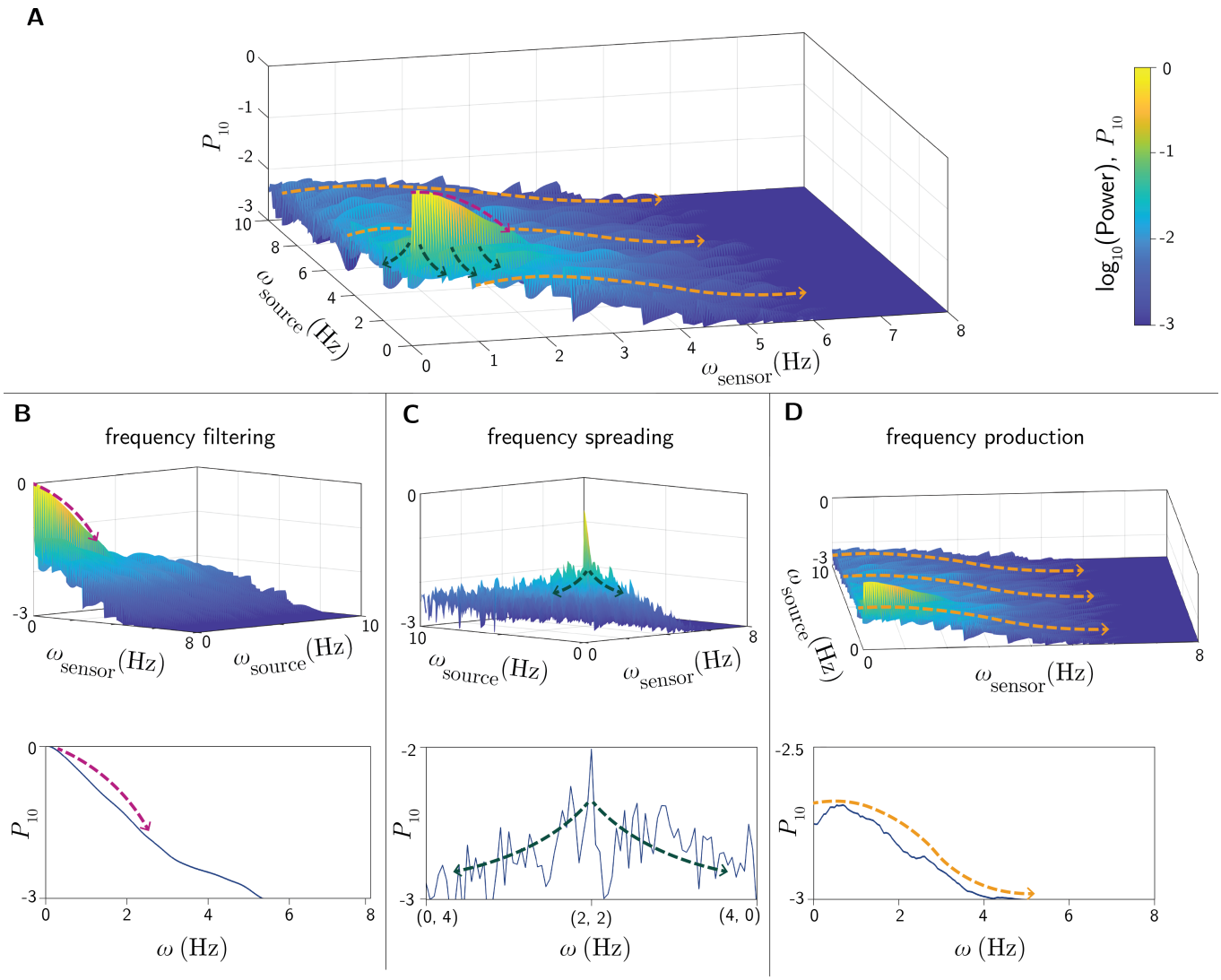

FIG. 4. Naturalistic case: example frequency mapping of an odor signal with a range of frequency content at the source, which is then transformed by turbulent transport to a different spectrum in the signal received at the sensor. This case shows an odorant with diffusivity 1.5×10^{-6} m^2/s, which is released at (0,0) then detected by a 0.031 m $\times$ 0.02 m sensor at a downstream distance of 0.05 m from the source (sensor 1 in Fig. 3). Each three-dimensional subplot is the same mapping matrix, shown from four perspectives: (A) a generic overview (B) along the axis of output frequency=input frequency, to highlight low-pass filtering of the source frequency (indicated by dashed red arrow);below is a transect along the diagonal from (0, 0) to (8, 8) (C) orthogonal to the view in (B), to highlight frequency spreading (indicated by dashed green arrows); below is a transect along the minor diagonal from (0, 4) to (4, 0), with the underlying spectrum subtracted (computed as the average spectrum for high frequencies largely unaffected by the source frequency) (D) a nearly top-down view, to highlight the similar underlying spectrum across many input frequencies (indicated by dashed gold arrows); below is the average spectrum for high frequency inputs of 20 to 25 Hz.

Chaotic flows, however, cause particles released at similar initial locations to separate at a rate much faster than if they only separated due to molecular diffusion. Such behavior can be modeled as a diffusive process with an *effective* diffusion coefficient based on particle separation rates, as first observed by Richardson [45]. We compute the effective diffusivity for our flow at each sensor location using the evolution of mean square particle separation rates, as explained in Appendix D. Further, we model the distribution of particle travel times to a given sensor using a lognormal distribution, based on the solution to the 1-D diffusion equation and consideration of the multiplicative stochastic processes in turbulence (see Appendix D). Fig. 5A plots the resulting lognormal distributions along with the observed first-order probabilities from the particle-tracking data. As shown, the lognormal distribution appears to be a good descriptor of the actual travel time distribution, with minor devi-

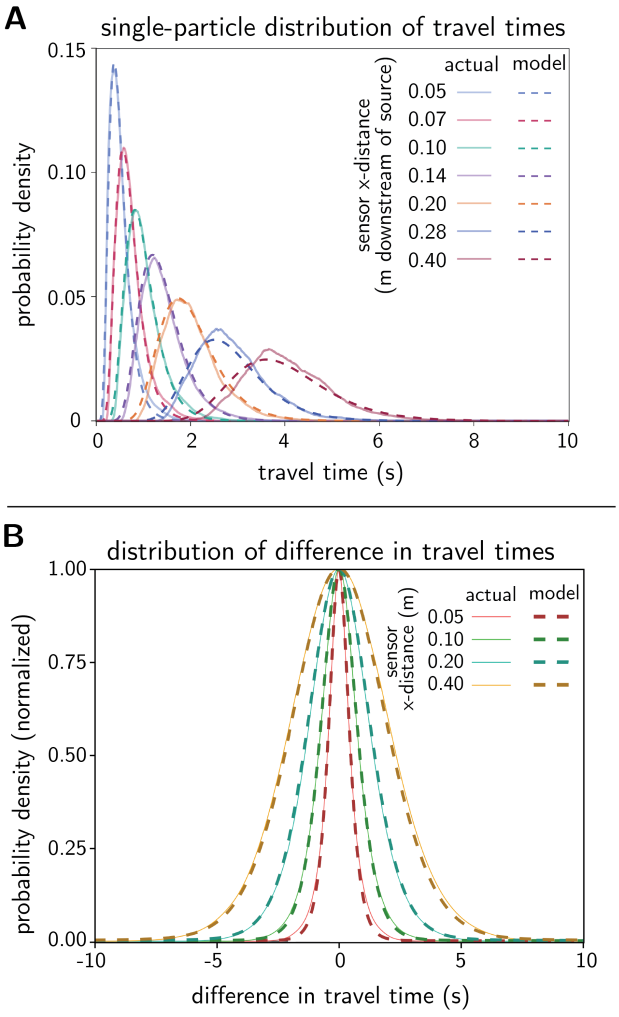

FIG. 5. Demonstration of effective diffusion model for explaining linear filtering behavior. (A) First-order travel time probabilities at seven sensor locations, as calculated from sensor detection occurrences in the data (solid lines) and as a lognormal distribution derived from flow properties (dashed lines). (B) Distribution of differences in travel times between two particles at four select sensor locations, as derived from constructing joint probabilities from the data (solid lines) and as the auto-covariance of the lognormal distribution derived from flow properties (dashed lines).

ations from the data that become more pronounced at locations further downstream.

Determining the frequency mapping then requires quantifying the joint probability of two particles having travel time 1 and travel time 2, given they are released some initial time difference apart. For modeling turbulent transport as a diffusion process, we make the assumption of independence; that is, the travel time of one particle has no dependence on the travel time of another. While a full description of particle pair dispersion would require consideration of the correlations between particle trajectories (which are dependent on the initial separation of the particles) [46], here we intentionally isolate the independent behavior to model the component of particle dispersion that acts analogously to molecular diffusion. Essentially, we invoke Richardson's assumption of locality to describe particle separations [47–49], deferring an investigation of the correlated aspects of particle pair trajectories for later sections. This assumption of independence allows us to compute the probability distribution of difference in travel times based on the autocovariance of the first-order probability distribution of travel time for each particle. The results of this computation are plotted alongside the actual distribution of travel time differences in our simulation in Fig. 5B. As illustrated, the computed distributions provide an excellent description for the observed data. We now have a physical explanation along with a method for computing the frequency filtering component of the mapping function.

Process 2: turbulent energy cascade spreads frequencies

Next, we provide a phenomenological explanation for the frequency spreading using the concept of the *energy cascade* in turbulent flows. As alluded to in the idealized frequency production case, the energy in a turbulent flow is distributed across length scales from relatively large energy-containing eddies (quantified in fluid dynamics by the *integral length scale*), to the smallest eddies that dissipate energy into heat (quantified by the *Kolmogorov microscale*). The energy in the flow transfers across these differently-sized eddies, described by their length scales, in generally predictable ways, at least in a statistical sense. Concretely, the distribution of energy across scales in a flow follows universal power laws through various length scale ranges (for sufficiently high Reynolds numbers; i.e., when there is a large scale separation between the energy containing and dissipating scales) [26]. These power scaling laws are well established in the field of fluid dynamics and we refer the interested reader to texts such as [50] and [51] for additional details and nuances. If the velocity spectrum in our chaotic flow simulation follows expected power laws, we can have confidence that the energy transfer behaves as expected, and that these energy transfers across scales would spread a transported odor signal spectrum across a wider range of frequencies.

To determine the velocity spectrum for the current simulation, we use the Fourier Transform of the fluctuating streamwise velocity spatial autocorrelation functions (based on Wiener-Khinchin theorem):

$$E(k) = 2\int_0^\infty R_{uu}(r)\cos(kr)\,dr, \tag{15}$$

where $R_{uu}(r) = \langle u'(x)\,u'(x+r)\rangle$ is the spatial autocorrelation function of the velocity fluctuations, k is the wavenumber (rad/m), and $E(k)$ represents the energy density per unit wavenumber. An example resulting flow

spectrum for a sensor position at 0.05 m downstream of the source (sensor 1 in Fig. 3) is shown in Fig. 6.

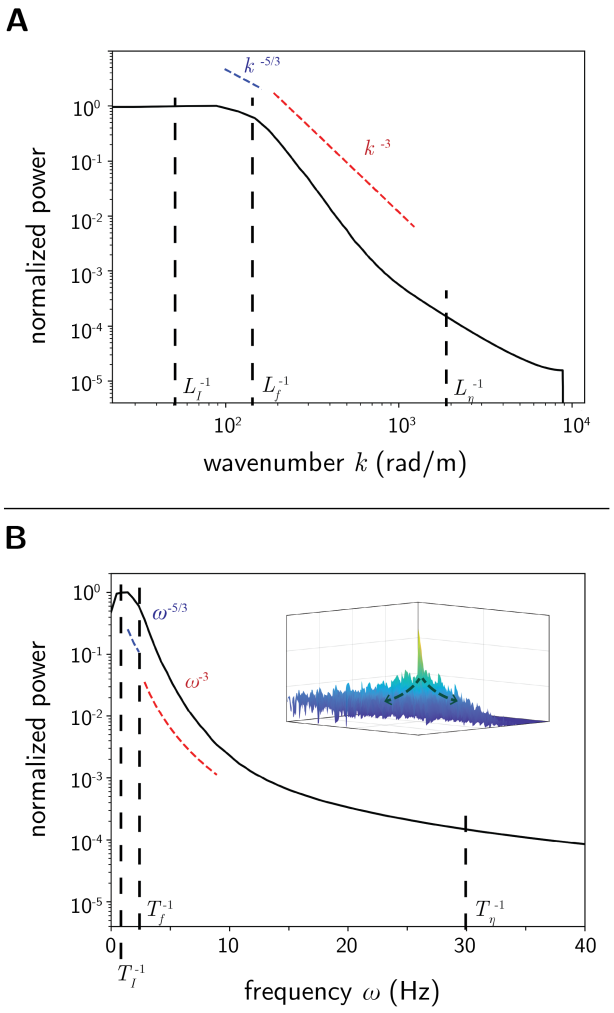

FIG. 6. Velocity spectrum for sensor at a downstream distance of 0.05 m, (A) shown in the traditional fluid dynamics form as a log-log plot with wavenumber k on the x-axis, and (B) shown in a more sensory-relevant form that mimics the mapping matrix format as a semilog plot with frequency on the x-axis. Red and blue dashed lines show expected power scaling in the inertial range. Relevant length (time) scales are shown as black dashed lines: integral scale is marked with subscript I, forcing scale with subscript f, and Kolmogorov scale with subscript η. A perspective plot of the frequency mapping function from Fig. 4C is inset in (B) to illustrate the component of frequency spreading.

While the velocity spectrum depends strongly on the specifics of the flow field, we can still identify characteristic patterns in the spectrum and compare them to expected behavior based on fluid dynamic principles. First, we examine the position of key length scales (here converted to wavenumber) relative to slope changes in the spectrum. We start by observing the position of the forcing scale, loosely interpreted as the size of eddies at which energy enters the system, in this case the spacing of the cylinders generating wake structures upstream of the source. Its location coincides approximately with the change from a slope of about -5/3 to a slope of about -3 in the power spectrum. This matches well-known behavior in fluid dynamics specific to two-dimensional flows, in which the forcing scale demarcates the transition between two distinct cascades: a reverse energy cascade and a forward enstrophy cascade, with power scalings of approximately -5/3 and -3, respectively. We observe that for this particular flow, the -5/3 section of the spectrum is present only for a very small range of wavenumbers, a behavior that reflects the location just a short distance downstream of the forcing (that is, the cylinder array) and the low Reynolds number that yields smaller scale separation in the flow, and which has been previously observed in similar 2D experimental flows [52]. Regarding other length scales, the integral scale is slightly larger than the forcing scale (i.e., positioned at a lower a wavenumber), since energy tends to accumulate at larger scales as the flow moves downstream from the cylinders. Finally, the Kolmogorov microscale is much smaller than the other scales, past the range of -3 power scaling to very small scales necessary for dissipation.

In natural flows, the velocity spectrum varies widely depending on the environmental conditions. A notable change lies in the fact that real-world flows are, by nature, three-dimensional, which is known to simplify the spectrum to a single energy cascade with power scaling of -5/3 for a range of wavenumbers, eliminating the dual-cascade and -3 scaling present in two-dimensional flows. In a given olfactory context, the specific length scales (i.e., wavenumber ranges of various parts of the spectrum) will be driven by parameters including the mean flow speed, any obstacles present (such as trees, grasses, rock formations, or landscape features), and height in the atmospheric boundary layer. Additional discussion of the velocity spectrum properties and expected changes under different conditions - including two-dimensional versus three-dimensional flows and plumes within turbulent boundary layers - is provided in Appendix A.

In terms of odor signal transformations, the spectral characteristics of the flow will determine the manner in which the power in odor signals is redistributed across neighboring frequencies. Due to the wide variety of length scales (and therefore frequencies) in natural flows, it may be advantageous for a particular species' sensory system to be tuned to frequencies in the typical spectrum of their expected environment for olfactory navigation tasks. More generally, the introduction of new frequencies to the odor signal benefits detection of odors through providing varied stimulus and thereby mitigating decreasing sensitivity from adaptation to a static odor concentration [16].

Process 3: frequency production imparts characteristic underlying spectrum

To explain the frequency production component of the reformatting behavior, we combine concepts of molecular diffusion and the turbulent energy cascade. For a simplified conceptual model, one can imagine that as an odor signal moves downstream, high-frequency information is "smeared out" by molecular diffusion; that is, the high frequency signal is transformed towards a zero-frequency, continuous signal. Then, the multi-scale interactions in the turbulent flow impart a new frequency distribution onto the now-continuous signal, as discussed in the idealized frequency production case. The combination of these processes results in the presence of a common underlying frequency spectrum with similar characteristics across many different input frequencies.

We can also situate the frequency production component within broader olfactory research that leverages the statistics of "whiffs" and "blanks" in odor signals, where whiffs are periods of time during which concentration is above some detectability threshold, and blanks are periods of clean air in between whiffs (see e.g. [11, 53, 54]). Understanding the statistical properties of whiffs and blanks has been used both to increase understanding of real-world odor signals [55] as well as to inform the development of laboratory protocols for naturalistic stimuli [28]. The statistics of such whiffs and blanks is directly related to the spectrum of the odor signal, and therefore, on the frequency production component of the odor signal transformation. Intuitively, one can think of low-frequency signals produced by large eddies in the flow as driving long on and off periods of concentration, resulting in the "clumping" or "bouts" of whiffs observed in odor plumes [56]. The production of higher frequencies (via relative dispersion from smaller eddies) then drives the fluctuations and durations of whiffs and blanks within these clumps. Detailed knowledge of the odor signal frequency spectrum may therefore be leveraged in a similar manner as whiff statistics to better understand natural signals and inform laboratory protocols.

In order to characterize the frequency distribution produced in the odor signal, we use the Batchelor spectrum shown in equation 11. As previously discussed, there are two terms in the equation: a power law scaling component and a diffusive cutoff term. The velocity spectrum from the previous section can be used to characterize the power scaling term: we found a -5/3 power scaling for frequencies in the inverse energy cascade (around $0.8 < \omega < 2$ Hz), and -3 scaling for frequencies in the forward enstrophy cascade (around $2 < \omega < 10$ Hz).

For estimating the diffusive cutoff component, $\exp(-\gamma\omega^2)$, we use dimensional arguments to provide a coarse estimate for the parameter γ. We expect molecular diffusion to become important only at very high wave numbers, and therefore the above-described velocity spectrum will dominate scalar variance production at the wave numbers of interest in the present application. For the purposes of this analysis, we can use the solution in eq. 5 as the exponential portion of the Batchelor spectrum, but this time with D as molecular diffusivity (rather than an effective diffusivity from particle separations):

$$\gamma \approx \frac{2Dx}{\overline{u}^3}. \tag{16}$$

We can now combine the diffusive and power scaling components of the Batchelor spectrum to develop an expression for the expected underlying odor signal spectrum observed across a wide range of input frequencies:

$$\langle \tilde{P}(\omega) \rangle = A\omega^{-\alpha} \exp\left[\frac{-2\omega^2 Dx}{\overline{u}^3}\right], \tag{17}$$

where α is -5/3 in the inverse energy cascade (around $0.8 < \omega < 2$ Hz), -3 in the forward enstrophy cascade (around $2 < \omega < 10$ Hz), with anomalous scaling for higher values of ω. The constant A is related to the relative strength of the correlated versus independent components of the total power spectrum and its estimation is beyond the scope of the current work (see the Discussion for further information on the issues involved). Fig. 7 compares the output spectrum of a high-frequency input with expected scaling behavior and with numerical results of the continuous-source case (at a distance of 0.40 m from the source, see sensor 7 in Fig. 3). As shown, the plots are in close agreement. The similarity between the continuous source spectrum and the high-frequency source spectrum illustrates how quickly high-frequency information is erased by molecular diffusion, resulting in an essentially continuous signal shortly after release, which is then transformed by the turbulent transport process. The introduction of new frequency content to an odor signal may benefit both detection and source localization tasks, as further discussed in Sec. III.

F. Effects of odorant diffusivity, sensor location, and sensor size

The sections above focus on illustrative examples to demonstrate the odor signal reformatting behaviors. In this section, replicating the analysis with variations to key parameters serves to both validate the consistency of the three primary processes described above as well as probe the effects of the parameter variations. The varied parameters include the odorant diffusivity, sensor location, and sensor size, with a quantitative evaluation of the impacts to the reformatting processes. In all these cases, we analyze odor sources that emit unsteady signals with a range of frequency content.

The time domain perspective provides a useful way to quantify the effects of parameter changes, as we can directly analyze the joint statistics of the particle pairs. Fig. 8A shows an example time domain plot of difference in travel time versus difference in release time. In

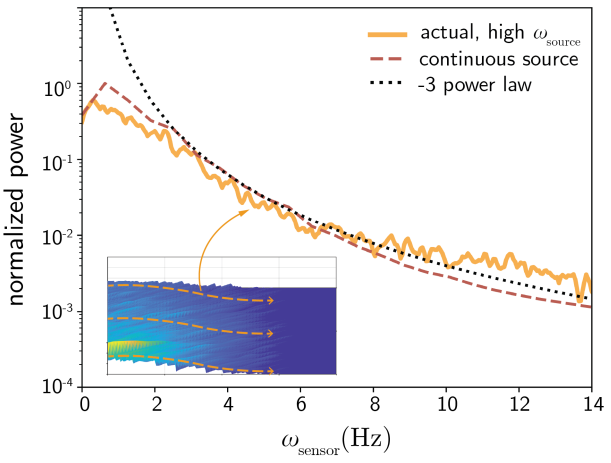

FIG. 7. Comparison of frequency production in particle tracking simulation to expected power law scaling and continuous source model results. Example shown is for an odor with diffusivity 1.5×10^{-5} m^2/s, released at (0,0) and detected by a 0.087 m $\times$ 0.02 m sensor at a downstream distance of 0.40 m from the source. The inset illustrates an entire mapping plot, from which the gold line is computed from averaging across high source frequencies. Specifically, the gold line shows the average spectrum of particle pairs released closely space in time, at a frequency of 20 to 25 Hz. The red dashed line shows results of a Fourier transform of the signal at the same location as directly modeled for the idealized continuous source case. Black dotted line shows ω^{-3}, scaled for comparison with the other two curves.

the time domain, the plot naturally partitions into two components: an 'independent component' that behaves identically regardless of difference in release time, and a 'correlated component' whose behavior *does* depend on the release time difference. To connect to our frequency-domain descriptors: the independent component represents the frequency filtering process, while the correlated component encompasses both the frequency spreading and frequency production processes.

For the independent component, the physics of diffusive processes allow us to build a mathematical model of the behavior, as previously described in the frequency filtering section. Once we obtain a model of the independent component, we can subtract it from the time domain plot to isolate the correlated component for parameterization. We are then left with a time-domain plot of the correlated component (the component related to frequency spreading and production).

As evident in Fig. 8A, the correlated component becomes important at small differences in release time. Intuitively, this can be thought of as particles that are closely spaced in time being released into a velocity field that is more likely to be correlated with itself, and therefore their trajectories are more likely to be correlated with each other. For reasons that we explore in the discussion, a complete quantification of the behavior of such correlated particles remains an open area of research in turbulence theory. In this section, then, we instead seek to parameterize the behavior under a range of conditions. Fitting Gaussian functions to the spread of travel time differences allows for quantitative comparison of the mean, standard deviation, and area under the curve for the Gaussian fits. The results displayed in Fig. 8B show these Gaussian parameters, compared across sensor locations (column 1), odorant diffusivities (column 2), and sensor sizes (column 3).

For the mean travel time difference (first row of Fig. 8B), we identify an approximately 1:1 ratio of mean shift to release time difference across all parameters, implying that particles released some small time apart 'catch up' with each other and arrive at the same time, on average. This seems to be a known phenomenon attributed to eddy sweeping and intermittency in velocity fluctuations for turbulent flows (see for instance [57, 58]), so we take it as an observed behavior of turbulence. The behavior implies that very high frequencies (i.e. small separation times) will not persist for long after release from the source, even neglecting the role of molecular diffusion.

Looking at the width of the Gaussians (standard deviation, second row of Fig. 8B), we note that the width gradually increases with increasing initial separation and is dependent on both sensor position and molecular diffusivity. In other words, the further the sensor is downstream of the source, the wider the curve, because particle pairs will show a larger spread in travel times the farther they have traveled. Increasing the molecular diffusivity (once it is high enough to be relevant) also increases the spread of travel times, since molecular diffusion can separate particles into different trajectories in the flow field. For a given odor signal, a wider spread in the travel time differences relates to the attenuation of high-frequency content, further emphasizing the inherently local nature of high-frequency information.

The area under the curve (third row of Fig. 8) represents the strength of the correlated component. At a difference in release time of zero, the area is at its maximum, then the area asymptotically approaches a small value by a difference in release time of about 0.2 seconds; note that 0.2 seconds is meaningful in that it is the integral scale of the flow near the source, which represents the time over which the flow is correlated with itself. In other words, this behavior shows that when particles are released at intervals longer than the integral time scale of the flow (meaning, into flow fields that are uncorrelated with each other), they mostly move independently and therefore have minimal power in the correlated component. Importantly, the decay does not go completely to zero, which means new frequencies are still produced in the signal, but that the relative power in those new frequencies is much smaller.

The curves also appear to scale directly with sensor cross-stream width, a parameter that we select during the analysis setup. As particles travel downstream, they spread laterally apart from one another, so a wider sen-

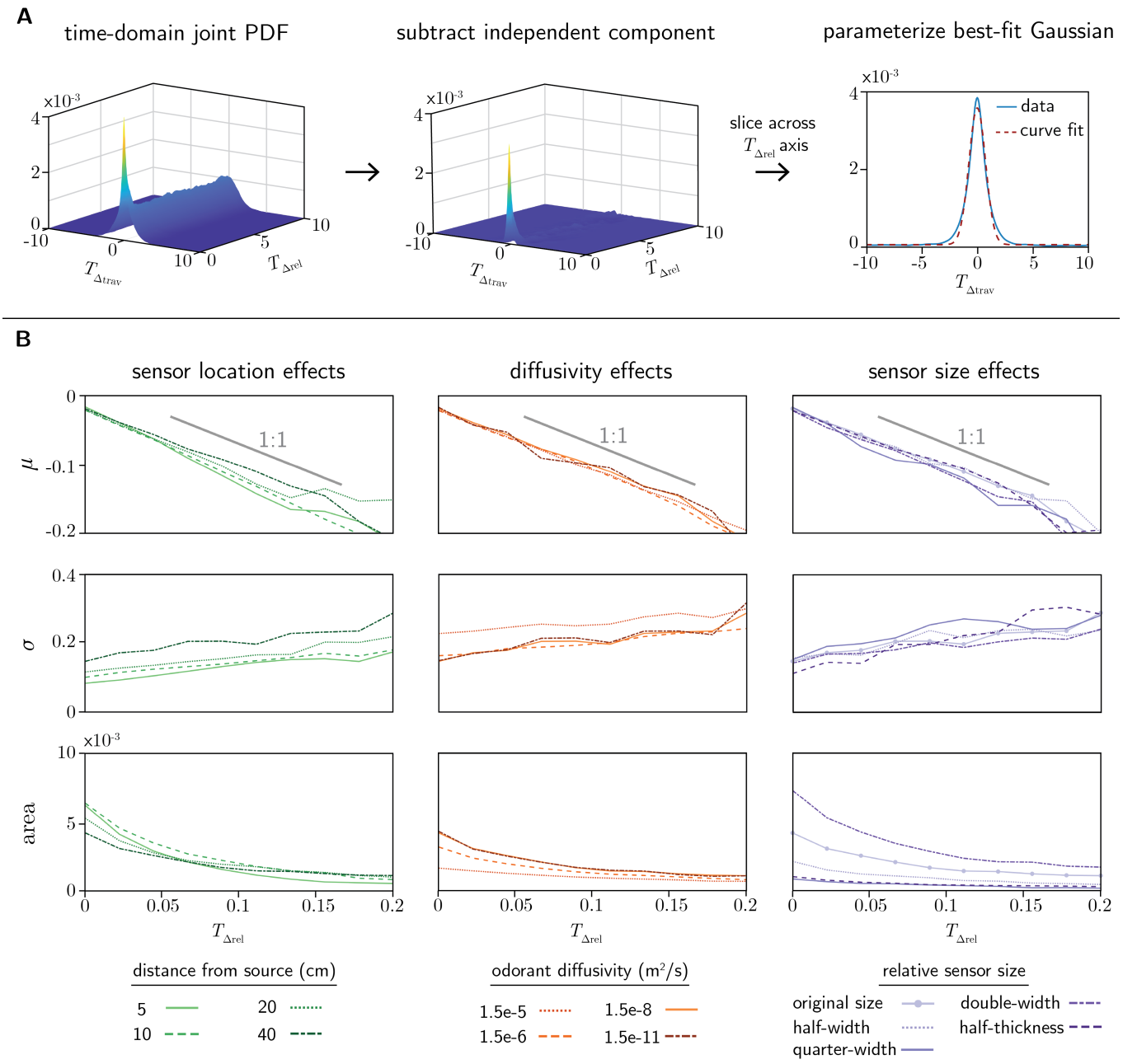

FIG. 8. Time-domain approach and results for parameterizing the correlated component of the frequency mapping function. (A) Analysis approach: first, we construct a time-domain plot of difference in travel time, $T_{\Delta\text{trav}}$, vs difference in release time, $T_{\Delta\text{rel}}$, for particle pairs. Next, the quantifiable independent component is subtracted, leaving a "spike" representing the correlated component, significant at small differences in release time. Finally, slices are taken along the $T_{\Delta\text{rel}}$ axis and Gaussian functions are fit to each curve using an iterative approach to minimize the χ^2 metric. (B) Resulting parameters characterizing a Gaussian fit to the correlated component of the time-domain mapping function for a range of small differences in release time. The top row shows the mean, μ, the middle row the standard deviation, σ, and the third row the area of the best-fit Gaussian function (computed as area $= A\sigma\sqrt{2\pi}$, where A is the amplitude). The first column shows the effects of moving the sensor to different downstream distances with diffusivity held constant at 1.5×10^{-5} m^2/s and sensors at the original size (2 cm thickness with the width scaling as $\sqrt{x_i/x_0}$). The second column measures effects from varying the odor diffusivity, at a location of 40 cm downstream and the original sensor size (0.087 m $\times$ 0.02 m at this location). Because there is constant kinematic viscosity across cases, this can also be thought of as varying the Schmidt number (Sc, a dimensionless number that quantifies the ratio of momentum diffusivity to mass diffusivity as Sc $= \nu/D$), from Sc $= 1$ to Sc $= 10^6$. Note that Sc of order unity represents typical air-borne odor conditions, while odors in water exhibit Sc on the order of 10^3 m^2/s, and a Sc of 10^6 is essentially a non-diffusive condition. The third column displays results of changing the sensor size, with diffusivity held constant at 1.5×10^{-5} m^2/s and sensor location at 40 cm downstream of the source.

sor detects more of these particles. More pertinently, a higher percentage of trajectories may be correlated with one another due to the sensor detecting additional particles that have correlated arrival times to some downstream distance, but be spread laterally wider than the original sensor. This finding has implications for sensor size in olfactory navigation - for instance, that a long antenna (on the scale of, say, a cockroach) may detect the correlations in the odor signal due to flow structures more strongly than a short antenna (on the scale of, for example, a fruit fly), for a given flow field.

III. DISCUSSION

A. Implications for sensing and olfactory navigation

The temporal structure of odor signals is known to be important for animal navigation [19, 59, 60]; therefore, characterizing the temporal reformatting of these signals represents an important step toward understanding the olfaction process. We design the current analysis in the context of real-world olfaction, in which arrays of sensory structures are located in an area of finite size (such as insect antennae or the olfactory epithelium in mammalian nasal cavities, see for example [61–64]), the flow is chaotic with a fluctuating velocity field [24, 65], and odor sources may fluctuate and emit signals with a range of frequency content [39, 66–68]. Despite the complexity of the problem analyzed, we observe a consistent set of three dynamic processes that transform the odor signal during transport: frequency filtering, frequency production, and frequency spreading.

These transformations of the frequency content of the odor signal likely provide a selective advantage to a navigating animal. Frequency production in particular may be advantageous, since receptors are generally more sensitive to fluctuating signals than static ones, so the introduction of new fluctuations likely increases receptor sensitivity to the odor signal [15, 16, 69]. The transformed frequency content of an odor signal may also potentially encode information about source location, since the transformations that we observe are location-dependent (for further discussion of information extraction from plumes, see [55, 70–72]). Specifically, as distance from the source increases, we observe more filtering of high-frequency source signals, additional power in the underlying spectrum rather than the source signal, and wider spreading of source frequencies. Broadly, this demonstrates that low-frequency signal content can persist far from the source. High-frequency content, on the other hand, is continually generated and destroyed in the turbulent transport process, and information in the high-frequency bands will have a more complex relationship with the source signal, as explored in [29]. Animals that find odors under specific conditions (for example, the typical mean wind speed and turbulence intensity in a densely treed forest will be different than those in open meadows) could, and may, benefit from receptors tuned to the frequency bands most relevant for their navigational context [54].

Let us also consider the implications of an animal that emits some odor signal with the goal of transmitting information to other animals (as in a female moth releasing pheromone pulses to attract mates). Low frequencies in the odor source spectrum persist farther downstream – flowers that slowly pulse their odor release may have the advantage as far as long-distance transmission of a low frequency signal [68]. However, if a navigating insect has some intuitive understanding of the frequency content of the source (say, the navigating moth knows the characteristic frequencies in the transmitted pheromone signal), then the frequency content of the signal may be informative for distance from the source. Concretely, in the far field, the frequency content largely reflects the flow, with only the lowest frequency content in the source signal persisting, but as the navigating insect approaches the source, more of the frequency content characteristic of the source is available to the navigator. So as the navigator approaches the source, the presence of unique frequency content of the source signal would indicate that it is drawing closer to the source. If, on the other hand, the insect detects the frequency signature of the source but then it 'disappears' from the odor signal spectrum, that would be an indication that the insect is moving farther from the source. One can imagine the advantage of a transmitting animal (for example, the female moth) emitting a signal containing a unique higher-frequency content spectrum that helps the navigator understand distance from the source in the relatively near field, but at a low-frequency duty cycle to transmit some information as far as possible. Source emission rates could also be modulated by wind speed or level of turbulence to either increase signal range or dissipate quickly, depending on the objective of the transmitting organism. Whether animals actually modulate release frequencies for these purpose, or if release rate is primarily a matter of biophysical constraints, is a matter of future research [39].

While the current work does not directly explore the above speculations, it sets up a framework for how one may analyze these questions in the future. We frame turbulent transport as an intrinsic part of the olfactory process: it is the first of a series of signal processing steps that an odor signal undergoes between release of the odor and the perception by an organism. After a signal is transformed by the flow, animal behavior may also change the frequency spectrum, through processes collectively known as *active sensing* [73]. Activities such as sniffing [74], antennal movements [75], and even wing beats [76] modify the flow and odor fields, re-weighting power across frequency bands. As an animal navigates, its locomotion also transforms the odor signal by altering the relative motion between the animal and the evolving odor field. Potentially, such activities can be leveraged to accentuate portions of the spectrum with higher in-

formation density, or with increased receptor sensitivity. Once odor reaches a receptor, transduction and processing represent additional signal processing steps [77, 78]. That is, we see odor transport as the first stage of a complex series of odor signal transformations that must be taken into account if we are to fully understand olfactory navigation.

B. Connections to turbulence literature

The dynamic processes that we identify closely parallel classical turbulence perspectives, but with conceptual re-framing to understand the transformations from a sensory-relevant signal processing perspective. Specifically, this work dovetails with fluid dynamics literature that outlines the processes governing both passive scalar variance and turbulent kinetic energy. Regarding passive scalar variance, the seminal work of Csanady (1967) derives a transport equation for the variance of a concentration field, $\langle C'^2 \rangle$ (also known as the mean square fluctuations), as:

$$\frac{\partial \langle C'^2 \rangle}{\partial t} + \langle u_i \rangle \frac{\partial \langle C'^2 \rangle}{\partial x_i} = -2\langle u_i' C' \rangle \frac{\partial \langle C \rangle}{\partial x_i} - \frac{\partial \langle u_i' C'^2 \rangle}{\partial x_i} - 2D \left\langle \frac{\partial C'}{\partial x_i} \frac{\partial C'}{\partial x_i} \right\rangle \quad (18)$$

where C is the concentration, u_i is the velocity, and a prime represents fluctuation from the mean. The terms on the left-hand side describe the total change in variance due to local changes-in-time and advective changes. On the right, we see terms that relate to our process decomposition: 1) variance production due to the interactions of the turbulent energy cascade and concentration gradients, 2) the divergence of variance flux due to turbulent transport (as in effective diffusion due to turbulent eddies), and 3) variance dissipation that sets the attenuation of fluctuations [79]. Note that in the formulation above, the divergence of variance flux due to molecular diffusion is assumed to be much smaller than that due to turbulent diffusion and is therefore not included in the second term on the right-hand side. The terms in the concentration variance equation map closely onto the physical processes known to transform turbulent kinetic energy (TKE) in a boundary or mixing layer - see [80] for an early example of derivation of the TKE equation. In the TKE balance equation, the analogous right-hand side terms represent production of TKE due to interactions between the Reynold stress and mean shear in the flow, the spatial transport of TKE by turbulent eddies, and the dissipation of kinetic energy by viscosity (additional details can be found in numerous fluid dynamic textbooks, for example [50]).

There are parallels between the three processes identified in the current work and the right-hand side terms in the variance budget (eq. 18). Regarding the first term, even though mathematically the production term remains a single process, we conceptually split the production term into our frequency *production* component that induces a spectrum based solely on the average rate of particle release (i.e., the underlying spectrum that looks similar across many source frequencies), along with our frequency *spreading* component that causes the energy to be spread across a cascade of frequencies adjacent to a given input frequency. For the variance turbulent transport term, we use effective diffusion coefficients to approximate the divergence of variance flux. The third term, related to variance dissipation, largely governs the relative power in the independent versus correlated components of our joint particle pair statistics; informally, the relative height of the diagonal ridge in our mapping plots compared to the underlying spectrum across the input frequencies. This term relates to yet-unsolved closure problems in turbulence theory, hence our empirical parameterization of the correlated component of the mapping function.

While the *processes* that we identify above are analogous to terms in classical literature that use an Eulerian formulation for scalar variance (that is, one that solves for the variance at a fixed location and time), our analysis *methods* more closely parallel formulations that take a Lagrangian approach to the problem (that is, one that tracks particles along their trajectories). Lagrangian approaches encompass a vast range of methods, but there is a class of models known as two-particle Lagrangian methods, first suggested by Durbin [81], that provides an especially relevant touch-point for the current study. A summary of such approaches can be found in [82] and [83]; here, we highlight two studies that investigate behavior of particular interest to the current investigation. Specifically analyzing a decaying turbulent flow, [84] developed PDFs of particle pair separations over time for particles released at zero separation, identifying trends similar to some of our observations, such as the broadening of the particle separation PDF with increasing time from particle release. Later, Yeung [85] analyzed particle pairs and their velocity correlations at different initial separations, but in isotropic turbulence with periodic boundaries, and found similar results to the current study in that the correlated component of particle pair statistics becomes important when the initial separation is small compared to the integral length scale. The present investigation differs from most existing two-particle Lagrangian studies by emphasizing conditions of interest in olfactory navigation contexts, in that we perform direct numerical simulations of a decaying turbulent flow field, allow for a fluctuating source to compute the concentration spectrum for a range of initial frequencies (or, viewed differently, a range of initial particle separations in time), and develop statistics for a finite-size detection area representing a sensor rather than statistics at a single spatial location. Additionally, we frame the analysis as an input-output mapping function, in line with the above view of turbulent transport as the first in a series of signal processing transformations.

As we alluded to when quantifying the behavior of correlated particles, the complete modeling of correlated particles in low-Reynolds number flows represents yet-unsolved problems in turbulence theory. Broadly, the problems relate to the persistence of initial condition effects as well as the linking of Eulerian and Lagrangian descriptors of turbulence. As described in [86], decreasing the initial time lags in Lagrangian particle pair analysis makes it necessary to consider dissipation effects, which then requires more nuanced and complex analysis. While numerous approaches exist to model such dissipation effects, they largely rely on system-specific parameterization of a micro-mixing time scale that is dependent on length and time scales in the flow along with source configuration including size and dimensionality [87, 88]. In fact, Benzi and Vulpiani [89] specifically point out that trying to use a few "critical phenomena" to characterize the scalar spectrum will never be completely accurate, since completely describing the scaling features would require an infinite set of exponents. In the current study, we are not interested as much in completely characterizing a generalizable odor spectrum, but rather in identifying a few of the most important physical phenomena relating to the signal reformatting. Therefore, we did not attempt to fully model this component but rather characterize the behavior with changes to relevant parameters. We use our empirical Gaussian parameterization (in terms of mean shift, width increases, and area decay with increasing separation in release times) to provide a bridge between Lagrangian pair statistics and observed frequency-domain mapping.

Finally, it is useful to identify phenomenological behaviors known in plume dispersion literature that affect the temporal reformatting of odor signals. Production of scalar variance primarily occurs in what is described as the "near-field" regime, located relatively close to the source, in which the plume width tends to be smaller than the characteristic length scales of the flow and the plume tends to behave in a meandering way, meaning the plume generally travels as a cohesive ribbon along the motion of large eddies in the flow [90]. In this regime, we expect the odor signal transformation to be dominated by the spreading of power across frequencies adjacent to each input frequency, and we expect the source configuration to be important, that is, for the spectrum to retain power in the original odor signal spectrum frequencies. By contrast, dissipation of scalar variance occurs primarily in the "far-field" regime, located at a large distance from the source, in which the plume tends to be wider than the characteristic length scales in the flow and relative dispersion dominates [91]. In this regime, we expect odor transformation to be characterized by rapid decay of small-scale fluctuations, interpreted as the attenuation of high-frequency signals in the frequency domain, and for source configuration effects to be largely "forgotten", that is, the spectrum to be mostly independent of the original odor signal spectrum. In the context of olfactory navigation, this means that encoding of source information (such as location and frequency content) is generally retained in the near-field spectrum, while the far-field spectrum largely reflects features of the transporting flow field.

C. Framework applicability and limitations

Due to their grounding in fundamental fluid dynamics principles and literature, we expect that the processes identified in this study will, in general, be widely applicable to other odor plume conditions. Specifically, the framework is directly applicable as long as the transport process itself is linear with respect to the odor concentration. This condition holds for the case for passive odor transport governed by the advection-diffusion equation, regardless of various parameter perturbations, such as varying the Reynolds number, turbulence intensity, or odor source characteristics. Further, the framework holds across both two-dimensional and three-dimensional flows, as well as for plumes within a turbulent boundary layer (or more generally, close enough to a boundary that wall effects are significant), as further discussed in Appendix A. However, deviations may arise in some cases, including very near surfaces that interact with odor in a concentration-dependent manner, and in the case of active scalars. Particularly relevant to olfactory navigation along the ground, surfaces exhibit odor-dependent nonlinearities in sorption processes that would in turn affect plume dynamics in very close proximity to the surface [13, 92, 93]. Nonlinearities may also occur in the case of active scalars (for example, particularly dense or buoyant plumes) wherein the odor itself changes the flow field dynamics during transport, although in naturalistic cases odor concentrations are typically low enough that there are negligible effects on the flow field [22]. We consider these two nonlinear cases in more detail in Appendix A. In the presence of such nonlinearities, an extension or modification to our framework would be required.

D. Summary and outlook

In this study, we provide a framework to bridge a sensory-relevant perspective of odor signal processing in the frequency domain with known processes in transport of a passive scalar in turbulent flow. We employ Lagrangian tracking of particle pairs and transform the joint probabilities of sensor detection into a frequency-domain mapping of the power spectrum at the source vs the power spectrum at the sensor. We then use fundamental fluid dynamics principles to identify the primary components of this mapping function. The results reveal three dominant processes that reformat the source signal as it is transported by turbulent flow: frequency filtering, frequency production, and frequency spreading. We model the frequency filtering effects using a simple diffusion model based on mean-square particle separations,

and demonstrate the frequency production and spreading components using the energy spectrum of the transported species, closely related to the energy cascade in the flow field. The relative contribution of these three components is a more nuanced matter that requires consideration of dissipation effects, which involves turbulence closure problems and is beyond the scope of this work.

Testing our findings in real-world naturalistic flows will clarify how universal the three-process decomposition is, and leveraging the findings in animal navigation research will reveal where biological systems may have evolved olfactory navigation policies that exploit it. Applying our framework to a wider range of flow conditions and source configurations will allow for further parameterization of the behavior of correlated particle pairs. Future studies focused on navigational policies or plume information can quantify what spectral features actually carry navigational value. For practical applications, coupling movement design to these mappings suggests new strategies for bio-inspired olfactory robots and testable behavioral predictions (for example, movement-induced frequency spreading or frequency-based distance estimation). The mapping function approach also provides a frequency-domain framework that can be extended to other transformations of the odor signal, including not only the transport process but also animal movement and active sensing, odor transduction, and neural processing. Viewing the entire journey of an odor as a series of signal processing steps, from release at the source to perception in the animal brain, allows for a concise description of sensory-relevant transformations in the odor signal frequency content. Within such a framework, we can then identify dominant transformations at each step, such as the three processes identified in this study for the transformation of odor signals by transport in turbulent flows.

ACKNOWLEDGMENTS

This work is supported by the National Science Foundation (USA), under the NSF/CIHR/DFG/FRQ/UKRI-MRC Next Generation Networks for Neuroscience Program (award number 2014217 to JPC) and the NSF GRFP (Grant number DGE2040434 to EAS). This work utilized the Blanca condo computing resource at the University of Colorado Boulder. Blanca is jointly funded by computing users and the University of Colorado Boulder. Data storage supported by the University of Colorado Boulder 'PetaLibrary'. JDV thanks the Kavli Institute for Theoretical Physics (KITP) and grant NSF PHY-2309135 for the opportunity to discuss this work at the Neurosensing 25 workshop.

DATA AVAILABILITY

The raw data that support the findings of this article are openly available [94].

IV. APPENDICES

Appendix A: Further discussion of framework applicability and limitations

Applicability to different flow regimes

The framework presented in the current work is generally applicable to changes in the flow field compared to our two-dimensional simulated flow, including three-dimensional flows and flows within a turbulent boundary layer. In this section we explore expected effects of these two example flow changes on the characteristics of the odor signal spectrum.

Even though the current study employs a 2D computational fluid dynamics simulation, there are well-known changes in the spectrum of 3D flows that allow us to anticipate behavior in a 3D context. In three-dimensional turbulence, energy is transferred from larger energetic eddies to smaller and smaller eddies until viscous dissipation as heat at the smallest scales, (the phenomenon known as the energy cascade, classically described by Richardson and formally stated by Kolmogorov in 1941 [26]). As shown in this study, two-dimensional flows exhibit a "dual cascade", due to conservation of enstrophy along with conservation of energy (enstrophy is defined as the one-half the mean square vorticity, a measure of rotation in the flow). In terms of physical mechanisms, in three-dimensional turbulence vortex stretching allows for the cascade of energy to smaller scales, while in two-dimensional flows vortex *gradient* stretching conserves the rotational quantity of enstrophy and allows it to cascade to smaller scales, while energy transfers to larger scales [95]. For the flow spectrum, this results in a dual-sided cascade from the forcing wavenumber: a backwards-energy cascade to smaller wavenumbers along with a forwards-enstrophy cascade to larger wavenumbers. In our mapping function context, for 3D flows we would expect the underlying spectrum to be reflective of the forward energy cascade and -5/3 power law scaling typical of 3D flows.

Similarly, even though we analyze a source in the center of a relatively large domain, minimizing boundary effects, the framework applies as the turbulent flow approaches a boundary (up until nonlinear sorption effects that may occur, as discussed in the following section). From fluid dynamics, we know that in such *turbulent boundary layers* concentration spectra are modulated with distance from the boundary, while still being transformed in a linear manner by the flow. Some of these changes are predictable, such as increased attenuation of high frequencies (strengthening of the frequency filtering component) near the boundary. This attenuation oc-

curs due to viscous effects, namely, that high shear near the wall smears out concentration fluctuations [96]. Due to the modulation of concentration spectra, we also expect that the relative importance of the filtering, spreading, and production components will shift with distance from boundaries. Experimental studies confirm this effect, showing, in general, an increase in the contribution of the filtering component and decrease of the production component as one begins moving from the freestream toward a boundary (subtleties related to this observation exist depending on the exact plume conditions and the distance from the wall) [97].

Sources of nonlinearity in odor transport

There are a few cases in which the framework does not fully capture the transformations to the odor and would therefore need to be extended or modified to apply. Specifically, the framework is no longer valid if the odor transport process shows nonlinear dependence on concentration of the odor. Below we explore two potential causes of this: if transport is occurring very near a surface with nonlinear sorption, or if the transported odor is not passive, but rather impacts the flow field as it is being transported.

Surfaces can play an important role in olfaction, especially in navigation tasks for walking organisms [92]. In such cases, odorant-specific sorption and desorption processes may alter the temporal dynamics of odor plumes [13]; such effects would necessarily introduce a nonlinear component to the spectral transformation of the odor signal and therefore not be described by the proposed framework. However, these effects are odorant-specific, and with odorants that have low concentrations or high desorption relative to adsorption to a given surface, the dynamics are expected to still be essentially linear [93]. Analysis of the specific effects and relative strength of this nonlinear component is out of the scope of the current work, but future research may help identify if the nonlinear effects have impact on navigation-relevant frequency information as in our signal processing framework, or primarily serve to discriminate between odors or identify olfactory objects [98–100]. We would also expect nonlinear effects of sorption to become insignificant within a short distance away from the surface, where the odor signal temporal dynamics would instead be dominated by linear turbulent transport processes.

Another case of nonlinearity would arise if the odor is no longer passively transported by the flow field. In such a case, feedback between the governing equations would result in nonlinear dependence on the concentration, so the framework of a linear mapping function would no longer hold. An example of an active scalar could be a particularly dense or particularly buoyant plume. In such a case, a body force term is introduced to the Navier-Stokes equations governing the velocity field of the transporting fluid, a term that itself depends on the odor concentration. A nonlinear dependence then arises when the concentration-dependent flow field is inserted into the concentration-dependent term of the advection-diffusion equation. In general, however, we expect odor plumes to be carried passively by the flow. Even though most common odorants are dense relative to air, typical plumes show low enough concentrations that any body forces are negligible and the framework still holds [22].

Appendix B: Effects of flow on power spectra: mathematical methods

1. Overview

This section presents a formalism for translating particle simulation data of a flow into quantities that characterize the transformation of the dynamics of odorant release at the source into the dynamics of odorant concentration at a downstream sensor. The primary goal is a quantity that describes how the power spectrum of odor concentration at the source is transformed into the power spectrum at the sensor.

We assume that an odorant is released into a flow at a single point, without perturbing the flow. The odorant concentration as a function of time is $s(t)$. A sensor is present at a fixed downstream displacement from to the source, and also is assumed not to perturb the flow.

An instance of the flow will be denoted by ϕ, each a member of an ensemble Φ. We seek to describe average behaviors. We will assume that the flow is statistically stationary and ergodic, i.e., that averages over $\phi \in \Phi$ are equivalent to averages over extended times – and moreover that averages over Φ may be estimated experimentally in this fashion.

2. First-order statistics

For an instance ϕ of the flow, denote the concentration time series at the sensor by $r_\phi(t)$. Then

$$r_\phi(t) = \int_0^\infty s(t-\tau) a_\phi(\tau; t) \mathrm{d}\tau \tag{B1}$$

where $a_\phi(\tau; t)$ is the fraction of odorant that was released at time $t - \tau$ that appears at the sensor at time t.The assumption that the odorant release does not perturb the flow implies that $a_\phi(\tau; t)$ is independent of the source time series $s(t)$.

Equation B1 also has a particle-tracking interpretation, which will be helpful for the analysis of second-order statistics: $s(t)$ is the probability that a particle in the flow is emitted at time t, $r_\phi(t)$ is the probability that the particle is at the sensor at time t, and $a_\phi(\tau; t)$ is the probability that a particle released at the source at time $t - \tau$ arrives at the sensor at time t.

The expected value of the sensor time series, i.e., its

ensemble average, is

$$r(t) \triangleq \langle r_\phi(t)\rangle_\Phi = \left\langle \int_{-\infty}^{\infty} s(t-\tau)a_\phi(\tau;t)\mathrm{d}\tau \right\rangle_\Phi \tag{B2}$$

where, here and below, $a_\phi(\tau;t)= 0$ for negative travel times τ. Since averaging is linear,

$$r(t) = \int_{-\infty}^{\infty} s(t-\tau)\langle a_\phi(\tau;t)\rangle_\Phi d\tau \tag{B3}$$

The assumption of ergodicity means that that averaging $a_\phi(\tau;t)$ over the ensemble is equivalent to averaging over absolute time t. Denoting this average by

$$a(\tau) \triangleq \langle a_\phi(\tau;t)\rangle_\Phi \tag{B4}$$

eq. B3 becomes

$$r(t) = \int_{-\infty}^{\infty} s(t-\tau)a(\tau)\mathrm{d}\tau \tag{B5}$$

That is, the average time series at the sensor is a linear transformation of the time series at the source. The kernel of the transformation, $a(t)$, may be regarded as an "impulse response" of the flow. It is natural to represent this relationship in the frequency domain,

$$\tilde{r}(\omega) = \tilde{s}(\omega)\tilde{a}(\omega) \tag{B6}$$

Here and below, we use standard Fourier transformation

$$\begin{cases} \tilde{x}(\omega) = \int_{-\infty}^{\infty} x(t)e^{-i\omega t}\mathrm{d}t \\ x(t) = \frac{1}{2\pi}\int_{-\infty}^{\infty} \tilde{x}(\omega)e^{i\omega t}\mathrm{d}\omega \end{cases} \tag{B7}$$

and the integral representation of the δ-function

$$\delta(u) = \frac{1}{2\pi}\int_{-\infty}^{\infty} e^{iuy}\mathrm{d}y \tag{B8}$$

which satisfies

$$f(x) = \int_{-\infty}^{\infty} f(u)\delta(u-x)\mathrm{d}u. \tag{B9}$$

3. Second-order statistics

To calculate the joint distribution of odorant concentrations at times t_1 and t_2, we maintain the particle viewpoint. We consider a scenario in which a particle of one odor is released with probability $s_1(t)$ and a particle of a second odor is released with probability $s_2(t)$, and compute the probability $z_\phi(t_1,t_2)$ that the two particles arrive at the sensor at times t_1 and t_2, respectively. We keep the identity of the odors represented by the two particles separate (this does not entail additional complexity) and later specialize to the case in which they are the same.

The two odor particles may have entered the flow at any pair of prior release times $t_1-\tau_1$ and $t_2-\tau_2$. The joint probability that two such particles arrive at the sensor after travel times τ_1 and τ_2 depends not only on these travel times, but may also depend on the difference between the release times, the absolute time (which we measure with respect to t_1, and on the instance of the flow. We denote this dependence by b_ϕ. Thus,

$$\begin{aligned} z_\phi(t_1,t_2) = \int_{-\infty}^{\infty}\int_{-\infty}^{\infty} & s_1(t_1-\tau_1)s_2(t_2-\tau_2) \\ & \cdot b_\phi(\tau_1,\tau_2,(t_2-\tau_2)-(t_1-\tau_1);t_1)\mathrm{d}\tau_1\mathrm{d}\tau_2 \end{aligned} \tag{B10}$$

where arguments of b_ϕ are the two travel times, the difference between the release of the first odorant's particle and the second odorant's particle (second particle minus first), and the absolute arrival time of the particle of the first odorant. $b_\phi = 0$ if either travel time τ_i is negative.

Again we can replace the ensemble-average with an average over time:

$$\begin{aligned} & z(t_1,t_2) \triangleq \langle z_\phi(t_1,t_2)\rangle_\Phi = \\ & \left\langle \int_{-\infty}^{\infty}\int_{-\infty}^{\infty} s_1(t_1-\tau_1)s_2(t_2-\tau_2) \right. \\ & \qquad \left. \cdot\, b_\phi(\tau_1,\tau_2,(t_2-\tau_2)-(t_1-\tau_1);t_1)\mathrm{d}\tau_1\mathrm{d}\tau_2 \right\rangle_\Phi \\ & = \int_{-\infty}^{\infty}\int_{-\infty}^{\infty} s_1(t_1-\tau_1)s_2(t_2-\tau_2) \\ & \qquad \cdot \left\langle b_\phi(\tau_1,\tau_2,(t_2-\tau_2)-(t_1-\tau_1);t_1)\right\rangle_\Phi \mathrm{d}\tau_1\mathrm{d}\tau_2 \\ & = \int_{-\infty}^{\infty}\int_{-\infty}^{\infty} s_1(t_1-\tau_1)s_2(t_2-\tau_2) \\ & \qquad \cdot\, b(\tau_1,\tau_2,t_2-t_1-\tau_2+\tau_1)\mathrm{d}\tau_1\mathrm{d}\tau_2 \end{aligned} \tag{B11}$$

where

$$b(\tau_1,\tau_2,\tau_{21}) \triangleq \langle b_\phi(\tau_1,\tau_2,\tau_{21};t_1)\rangle_\Phi \tag{B12}$$

since the ensemble average must be independent of absolute time. $b(\tau_1,\tau_2,\tau_{21})$ is a description of the pairwise statistics of particle flow: the joint probability of particles with travel times τ_1 and τ_2 arriving at the sensor, given that their release times (positive if particle 2 is released after particle 1) differ by τ_{21}.

To express eq. B12 in the frequency domain, we calculate its Fourier transform, in terms of

$$\tilde{s}_i(\omega) = \int_{-\infty}^{\infty} s_i(t) e^{-i\omega t} \mathrm{d}t \tag{B13}$$

and

$$\tilde{b}(\omega_1, \omega_2, \lambda) = \int_{-\infty}^{\infty}\int_{-\infty}^{\infty}\int_{-\infty}^{\infty} b(\tau_1, \tau_2, \tau_{21}) e^{-i\omega_1\tau_1 - i\omega_2\tau_2 - i\lambda\tau_{21}} \mathrm{d}\tau_1 \mathrm{d}\tau_2 \mathrm{d}\tau_{21}. \tag{B14}$$

From eq. B11,

$$\begin{aligned} z(t_1, t_2) = \frac{1}{(2\pi)^5} \int_{-\infty}^{\infty}\ [7\times]\ \int_{-\infty}^{\infty} & \tilde{s}_1(u_1) e^{iu_1(t_1-\tau_1)} \\ & \cdot \tilde{s}_2(u_2) e^{iu_2(t_2-\tau_2)} \\ & \cdot \tilde{b}(\omega_1, \omega_2, \lambda) e^{i\omega_1\tau_1 + i\omega_2\tau_2 + i\lambda(t_2 - t_1 - \tau_2 + \tau_1)} \\ & \mathrm{d}u_1 \mathrm{d}u_2\, \mathrm{d}\omega_1 \mathrm{d}\omega_2\, \mathrm{d}\lambda\, \mathrm{d}\tau_1 \mathrm{d}\tau_2 \end{aligned} \tag{B15}$$

The integral over τ_1 yields $2\pi\delta(-u_1 + \omega_1 + \lambda)$ and the integral over τ_2 yields $2\pi\delta(-u_2 + \omega_2 - \lambda)$, so

$$\begin{aligned} z(t_1, t_2) = \frac{1}{(2\pi)^3} \int_{-\infty}^{\infty}\int_{-\infty}^{\infty}\int_{-\infty}^{\infty} & \tilde{s}_1(\omega_1 + \lambda) \tilde{s}_2(\omega_2 - \lambda) \\ & \cdot \tilde{b}(\omega_1, \omega_2, \lambda) e^{i\omega_1 t_1 + i\omega_2 t_2} \mathrm{d}\omega_1 \mathrm{d}\omega_2 \mathrm{d}\lambda. \end{aligned} \tag{B16}$$

Comparing eq. B16 with

$$z(t_1, t_2) = \frac{1}{(2\pi)^2} \int_{-\infty}^{\infty}\int_{-\infty}^{\infty} \tilde{z}(\omega_1, \omega_2) e^{i\omega_1 t_1 + i\omega_2 t_2} \mathrm{d}\omega_1 \mathrm{d}\omega_2 \tag{B17}$$

yields

$$\tilde{z}(\omega_1, \omega_2) = \frac{1}{2\pi} \int_{-\infty}^{\infty} \tilde{s}_1(\omega_1 + \lambda) \tilde{s}_2(\omega_2 - \lambda) \tilde{b}(\omega_1, \omega_2, \lambda) \mathrm{d}\lambda. \tag{B18}$$

4. Cross-spectrum and power spectrum

If the release process is stationary, we can use eq. B18 to relate the cross-spectrum at the sensor to the cross-spectrum at the source. In this circumstance, the cross-correlation function for particle release depends only on the release interval:

$$\langle s_1(t + T_1) s_2(t + T_2) \rangle_\Phi = C_{\mathrm{source}}(T_1 - T_2) \tag{B19}$$

The cross- spectrum at the source, $\tilde{C}_{source}(\omega)$, is the Fourier transform of the cross-correlation

$$\tilde{C}_{\mathrm{source}}(\omega) = \int_{-\infty}^{\infty} C_{\mathrm{source}}(T) e^{-i\omega T} dT. \tag{B20}$$

As is standard to avoid diverging integrals, we assume that the particle release occurs only over a finite time interval $[-L/2, L/2]$, and consider the limit as $L \to \infty$. In this scenario, the cross-spectrum at the source is given by

$$\lim_{L\to\infty} \frac{1}{L} \tilde{s}_1(\omega_1) \tilde{s}_2(\omega_2) = \begin{cases} \tilde{C}_{\mathrm{source}}(\omega_1),\ \omega_1 + \omega_2 = 0 \\ 0,\ \text{otherwise} \end{cases} \tag{B21}$$

and the cross-spectrum at the sensor, $\tilde{C}_{\mathrm{sensor}}(\omega)$, satisfies

$$\lim_{L\to\infty} \frac{1}{L} \tilde{z}(\omega_1, \omega_2) = \begin{cases} \tilde{C}_{\mathrm{sensor}}(\omega_1),\ \omega_1 + \omega_2 = 0 \\ 0,\ \text{otherwise} \end{cases} \tag{B22}$$

Combining eq. B18 and B22:

$$\lim_{L\to\infty} \frac{1}{L} \tilde{z}(\omega_1, \omega_2) = \begin{cases} \frac{1}{2\pi} \int_{-\infty}^{\infty} \tilde{C}_{\mathrm{source}}(\omega_1 + \lambda) \tilde{b}(\omega_1, \omega_2, \lambda) \mathrm{d}\lambda,\ \ \omega_1 + \omega_2 = 0 \\ 0,\ \text{otherwise} \end{cases} \tag{B23}$$

For the nonzero case of eq. B23,

$$\lim_{L\to\infty} \frac{1}{L} \tilde{z}(\omega, -\omega) = \frac{1}{2\pi} \int_{-\infty}^{\infty} \tilde{C}_{\mathrm{source}}(\omega + \lambda) \tilde{b}(\omega, -\omega, \lambda) \mathrm{d}\lambda, \tag{B24}$$

which, in view of eq. B22, yields

$$\tilde{C}_{\mathrm{sensor}}(\omega) = \frac{1}{2\pi} \int_{-\infty}^{\infty} \tilde{C}_{\mathrm{source}}(\omega + \lambda) \tilde{b}(\omega, -\omega, \lambda) \mathrm{d}\lambda. \tag{B25}$$

When the odorants corresponding to the two particles are identical, the cross-spectrum becomes the power spectrum, so eq. B25 is also the relationship between the power spectrum at the source and the power spectrum at the sensor:

$$\tilde{P}_{\mathrm{sensor}}(\omega) = \frac{1}{2\pi} \int_{-\infty}^{\infty} \tilde{P}_{\mathrm{source}}(\omega + \lambda) \tilde{b}(\omega, -\omega, \lambda) \mathrm{d}\lambda. \tag{B26}$$

An important special case is that of a constant odor release rate. In this case, the power spectrum of the source is concentrated at a frequency of 0:

$$\tilde{P}_{\mathrm{source}}(\omega) = 2\pi \tilde{P}_0 \delta(\omega). \tag{B27}$$

Eq. B26 then yields

$$\tilde{P}_{\mathrm{sensor}}(\omega) = \tilde{P}_0 \tilde{b}(\omega, -\omega, -\omega). \tag{B28}$$

Note that the transformation B26 between the power spectra at the source and the sensor depends only on a restricted set of values for $\tilde{b}$. To focus on these values, we define

$$\tilde{B}(\omega,\lambda) \triangleq \tilde{b}(\omega,-\omega,\lambda) \tag{B29}$$

and use $\tilde{B}$ in the main manuscript. In terms of $\tilde{B}$, eq. B26 becomes

$$\tilde{P}_{\text{sensor}}(\omega) = \frac{1}{2\pi}\int_{-\infty}^{\infty} \tilde{P}_{\text{source}}(\omega+\lambda)\tilde{B}(\omega,\lambda)\mathrm{d}\lambda. \tag{B30}$$

5. Idealized cases

The main manuscript considers three idealized cases in which eq. B30 has a simplified form.

In the "frequency filtering" scenario, particles move independently. That is,

$$b(\tau_1,\tau_2,\tau_{21}) = a(\tau_1)a(\tau_2) \tag{B31}$$

so (from eq. B14)

$$\tilde{b}(\omega_1,\omega_2,\lambda) = 2\pi\tilde{a}(\omega_1)\tilde{a}(\omega_2)\delta(\lambda), \tag{B32}$$

$$\tilde{B}(\omega,\lambda) = 2\pi|\tilde{a}(\omega)|^2\delta(\lambda), \tag{B33}$$

and eq. B30 becomes

$$\tilde{P}_{\text{sensor}}(\omega) = \int_{-\infty}^{\infty} \tilde{P}_{\text{source}}(\omega)|\tilde{a}(\omega)|^2\delta(\lambda)\mathrm{d}\lambda \tag{B34}$$

$$= \tilde{P}_{\text{source}}(\omega)|\tilde{a}(\omega)|^2. \tag{B35}$$

In the "frequency spreading" scenario, the transport time for all particles is some fixed τ_0 , but the probability that two particles both arrive at all, $q(\tau_{21})$, depends on the interval between their release. In this case,

$$b(\tau_1,\tau_2,\tau_{21}) = \delta(\tau_1-\tau_0)\delta(\tau_2-\tau_0)q(\tau_{21}). \tag{B36}$$

From eq. B14,

$$\tilde{b}(\omega_1,\omega_2,\lambda) = e^{-i\omega_1\tau_0}e^{-i\omega_2\tau_0}\tilde{q}(\lambda), \tag{B37}$$

so

$$\tilde{B}(\omega,\lambda) = \tilde{q}(\lambda), \tag{B38}$$

and B30 becomes a convolution:

$$\tilde{P}_{\text{sensor}}(\omega) = \frac{1}{2\pi}\int_{-\infty}^{\infty} \tilde{P}_{\text{source}}(\omega+\lambda)\tilde{q}(\lambda)\mathrm{d}\lambda. \tag{B39}$$

In the "frequency production" scenario, the release process is constant. That is, the power spectrum of the source is concentrated at a frequency of 0 such that $\tilde{P}_{source}(\omega) = 2\pi P_0\delta(\omega)$. In this case, eq. B30 becomes

$$\tilde{P}_{sensor}(\omega) = \tilde{P}_0\tilde{B}(\omega,-\omega). \tag{B40}$$

Appendix C: Computational Fluid Dynamics model: details and validation

We performed the numerical simulations for the velocity and concentration fields used in our analyses via finite element discretization of the governing equations. To construct a chaotic velocity field, we simulated two-dimensional grid-turbulence using a mixing grid cylinder array in a rectangular domain measuring 0.6 m in the cross-stream (y) direction by 0.75 m in the streamwise (x) direction, plus a 0.12 m flow development section at the inlet. We modeled the resulting velocity field using a direct numerical simulation of the Navier-Stokes and continuity equations with a finite element method to discretize the problem and solve the partial differential equations. A version of this model was first developed for [29] and expanded spatially and temporally for this study. See Fig. 3 for a schematic of the model domain and table I for a summary of model geometry and parameters.

Initial conditions were set to zero velocity and pressure everywhere. The inlet velocity was ramped from 0 to U_0 over a short time interval to ensure solver stability. Boundary conditions were no-slip conditions at the cylindar walls and lateral domain walls (velocity=0), a uniform flow at the inlet, and zero pressure at the outlet. The uniform inlet flow was passed across the cylinder mixing array to create a chaotic flow field from the interacting cylinder wakes, which was iteratively solved for at each time step using the direct PARDISO solver, a time-dependent solver known for its stability that uses an implicit backward differentiation formula method and parallelizes the solving of sparse systems of equations [101]. An unstructured finite-element mesh was locally refined in areas with large velocity gradients, namely in the vicinity of the mixing cylinders and domain walls, to ensure that the finest expected dynamic scales were resolved. Specifically, the domain was discretized into 2,092,784 total triangular and quadrilateral elements with a maximum size of 2 mm and minimum size of 0.2 mm (average of 405 elements per square cm). The data was then exported onto a grid with 500 μm resolution, using Lagrangian shape functions for weak-form discretization of the velocity field between model elements. Each simulation was 180 s in duration, plus a 10 s flow development period to ensure chaotic flow conditions across the full domain.

The concentration field was modeled at the same time as the velocity field in our finite element model (we simply did not use the concentration information when performing particle tracking analysis). Similar to the velocity field, the model iteratively solved for concentration at each timestep using the time-dependent PARDISO solver, this time to solve the non-reactive advection-diffusion equation (equation D2) for each mesh element. We set the diffusion coefficient for the odorant to 1.5×10^{-5} m^2/s, equivalent to a Schmidt number of about 1. The source concentration was set to 1

Model property and units	Value
simulation duration (s)	180
total domain size (m, x x y)	0.87 x 0.6
inlet section length, plume domain length (m)	0.12, 0.75
small cylinder diameter (m)	0.01
large cylinder diameter (m)	0.015
cylinder spacing, center-to-center (m)	0.025
mean flow speed $\overline{u}$ (m/s)	0.1
fluid kinematic viscosity ν (m^2/s)	1.50E-05
Taylor Reynolds number (avg) Re_λ	130
exported spatial resolution (μm)	500
temporal resolution (s)	0.02

TABLE I. Summary of velocity field numerical model parameters and geometry. Taylor Reynolds number was computed as $\mathrm{Re}_\lambda = u'\lambda/\nu$, where λ is the Taylor microscale, computed as $\lambda = \langle \mathbf{u}' \rangle_{\mathrm{rms}} \sqrt{15\nu/\epsilon}$.

mol/m^3 and the source width 0.005 m. We set the initial concentration field to $C = 0$ across the entire domain. The odor source was ramped over a small time to C=1 mol/m^3 and held at a constant concentration thereafter, where the source profile along $x = 0$ was a smoothed top hat. Boundary conditions for the mixing grid and lateral walls were zero total odor flux normal to the surfaces, $-\mathbf{n} \cdot (\mathbf{J} + \mathbf{u}^* C) = 0$, with advective flux $\mathbf{u}C$, diffusive flux $\mathbf{J} = -\mathbf{n} \cdot D\nabla C$, and $\mathbf{n}$ as the normal unit vector. At the inlet and outlet, the boundary conditions were set to no diffusive flux normal to the boundary, $-\mathbf{n} \cdot \mathbf{J} = -\mathbf{n} \cdot D\nabla C = 0$. Like the velocity field, the concentration field was exported onto a 500 μm grid using Lagrangian shape functions for discretization.

Select summary statistics for the CFD simulation are plotted in Fig. 9. As shown in the top row of Panel **A**, the time-averaged concentration field shows smooth variation across the domain, decreasing rapidly as x increases and with distance from the centerline (note the log scale of the color bar). The time-averaged velocity field is essentially uniform across the bulk of the domain, approximately equal to the inlet velocity of 0.1 m/s. Due to the no-slip boundary conditions on the top and bottom walls of the domain, areas adjacent to these walls show expected boundary effects, informing our selection of domain width to minimize effects to particle transport statistics for sensors along the centerline. The instantaneous concentration and velocity fields show dramatically different structures that may vary sharply across the domain due to the fluctuating nature of the fields, as illustrated along the bottom row of Panel **A**.

We quantify two properties related to the turbulence characteristics of the velocity field in Panel **B**: integral time scale and turbulent kinetic energy. Both begin with Reynolds decomposition of the flow field into its time-average ($\overline{u_i}$) and fluctuating components ($u_i' = u_i - \overline{u_i}$). Turbulent kinetic energy was then computed as half the sum of squares of the fluctuating components:

$$\mathrm{TKE} = \frac{1}{2}\left(\overline{u'^2} + \overline{v'^2}\right).$$

As illustrated, the cylinder array generates a high amount of turbulent kinetic energy, which decays with distance from the array. For the integral time scale, we first computed the discrete autocorrelation R for positive lags k of the x-direction fluctuating velocity time series at each location as

$$R_k = \frac{\sum_t u'_{t+k} u'_t}{\sum_t u'_t u'_t} \tag{C1}$$

where the normalization ensures a value of unity at a lag of zero. To mitigate numerical noise in the autocorrelation function after the initial decay, we fit a Gaussian function from lag zero to the point at which R decayed to $0.4R_0$. In fluid dynamics literature, either exponential or Gaussian functions are commonly used for autocorrelation fitting in integral scale computations (for example, both shapes are considered in Klein [102]); we observed flattening of slope of the autocorrelation near zero lag (consistent throughout the domain), which informed our selection of a Gaussian fit. Least-squares optimization determined the fit parameters, implemented through the SciPy 'optimize' module in Python. Following curve fitting, we determine the integral length scale, T_I, based on analytical integration of the Gaussian:

$$T_I = A\sigma \frac{\sqrt{\pi}}{2} t_\Delta \tag{C2}$$

where A and σ are the fit parameters for the Gaussian function's amplitude and standard deviation, respectively, and t_Δ is the time between each value in the time series.

Appendix D: Effective diffusivity calculations

First we demonstrate the validity of using Richardson pair dispersion concepts to understand the independent component of the spectral transformation. We do so through inspection of the growth rate of particle pair separations for the particle tracking simulation. The ensemble-averaged mean square particle pair separations for various initial separations are shown in Fig. 10. The initial separation distance, r_0, is estimated based on the time between releases and average flow velocity. Panel A shows cases with large initial separations, that is, those with $r_0 > L_0$, where L_0 is the largest length scale in the flow (set as the integral length scale near the downstream outlet of the domain). Panel B shows cases with small initial separations - those with $r_0 < L_\mathrm{I}$, where L_I is the energy injection length scale (taken as the integral length scale at the upstream end of the domain). We overlay dashed lines following expected scaling laws, including black lines with slope t^2, a red line with growth that is exponential in t, and purple lines with slope $\langle\epsilon\rangle t^3$, where ϵ decays as $t^{-3/2}$. Equations for expected scaling laws can be found in [103], along with details regarding

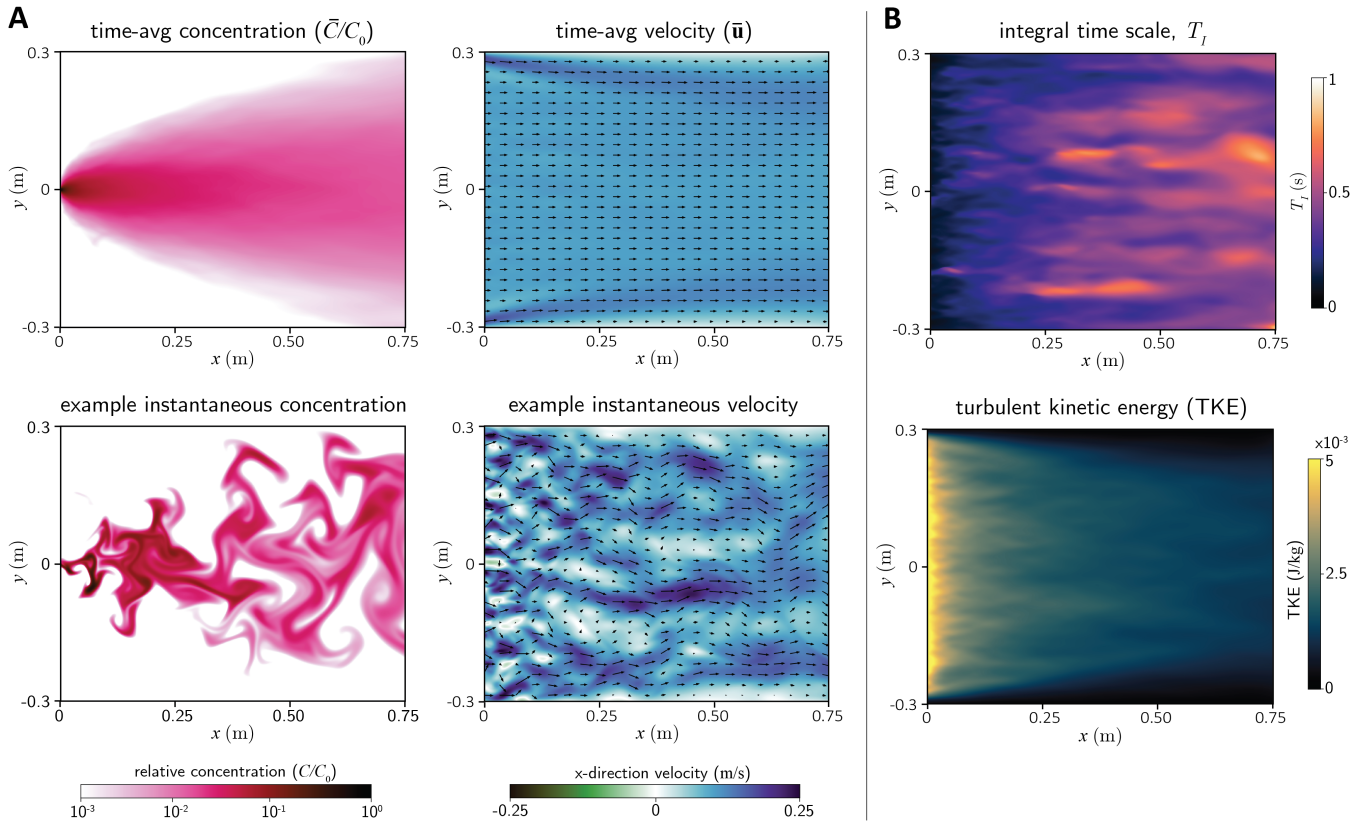

FIG. 9. Spatial distribution of properties computed for the computational fluid dynamics simulation, including: (A) time-average (top) and instantaneous snapshots (bottom) of the concentration and velocity fields, and (B) two time-averaged velocity field quantities: integral time scale and turbulent kinetic energy.

scaling of mean square particle pair separations in 2D versus 3D flows.

The enstrophy dissipation rate ϵ used in Fig. 10 was computed as:

$$\epsilon = 2\nu\langle E_{ij}E_{ij}\rangle \tag{D1}$$

where E_{ij} is the strain rate tensor of the fluctuating velocity field. Due to our decaying grid turbulence conditions, ϵ decreases downstream approximately as $t^{-3/2}$, as shown in Fig. 11.

In the simplest case for computing effective diffusivity, all sensors would be located far enough downstream that initial particle separations have been 'forgotten', so that there is a single value for mean squared separation regardless of initial condition. Note that our sensor locations are in the range 0.05 m (about 0.5 s average travel time) and 0.4 m (about 4 s average travel time), which lies in a regime where all initial conditions show similar particle separation rates (i.e., a constant slope). However, at the sensors closest to the source with small initial particle separations, there is some variation in the growth rate of mean square particle separation, so we expect some deviation from Richardson diffusion behavior in those cases.

To compute D_{eff}, we approximate the travel time as sensor distance divided by mean velocity. Then we can use Fig. 10 to find the mean square particle separation, then divide by the approximate travel time to obtain D_{eff}. By convention, a factor of 1/4 is included to align with the standard 1D solution to the advection diffusion equation:

$$C(x,t) = \frac{M}{\sqrt{4\pi D_{\text{eff}} t}} \exp\left[-\frac{(x-\mu)^2}{4D_{\text{eff}}t}\right], \tag{D2}$$

where C is the concentration and M is the initial mass, which we will take to be unity for the remainder of the analysis. Converting to our approximation of a Gaussian in time (see eq. D2) yields

$$C(x,t) \approx \frac{1}{\sqrt{4\pi D_{\text{eff}} x/\overline{u}^3}} \exp\left(-\frac{(t-x/\overline{u})^2}{4D_{\text{eff}}x/\overline{u}^3}\right). \tag{D3}$$

Furthermore, multiplicative random processes typically exhibit lognormal distributions, and indeed previous research in turbulent flows has identified lognormal distributions for concentration PDFs ([104–106]). We therefore expect that the first-order probabilities for particle travel times will follow a lognormal distribution with an underlying normal distribution that follows the above space-time conversion of the 1D solution to the advection-diffusion equation. We estimate the first-order

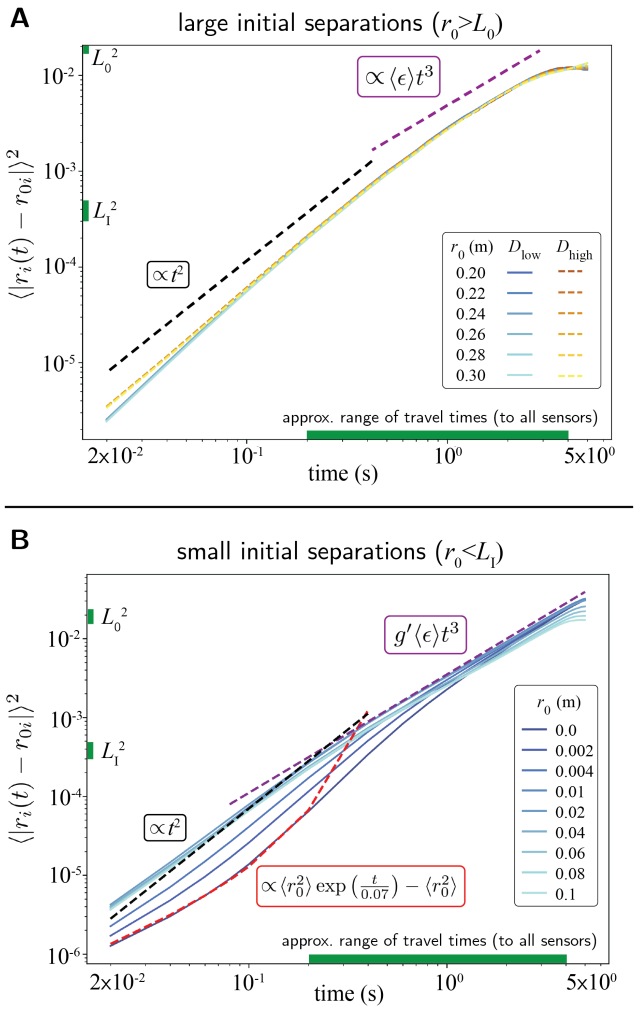

FIG. 10. Mean square particle pair separations computed from trajectory data.

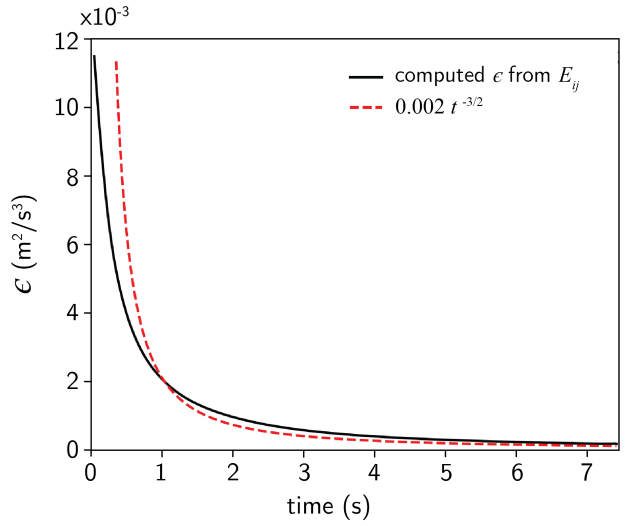

FIG. 11. Enstrophy dissipation rate demonstrating scaling approximately as $t^{-3/2}$.

x_s, m	μ_χ, s	$\langle\lvert r_{\mu_\chi} - r_0\rvert\rangle^2$, m^2	σ_χ^2, s^2	μ	σ	Scaling
0.05	0.5	0.0010	0.05	-0.78	0.43	0.064
0.0707	0.707	0.0016	0.08	-0.42	0.39	0.065
0.1	1	0.0028	0.14	-0.07	0.36	0.067

probabilities, $a_0(t)$, as a lognormal distribution with PDF:

$$f(t_{\text{travel}}; \mu, \sigma) = \frac{1}{t\sigma\sqrt{2\pi}} \exp\left(-\frac{(\ln t - \mu)^2}{2\sigma^2}\right) \tag{D4}$$

$$\text{for } t \in (0, +\infty) \tag{D5}$$

with mean (μ) and variance (σ^2) computed as

$$\mu = \ln\left(\frac{\mu_\chi^2}{\sqrt{\mu_\chi^2 + \sigma_\chi^2}}\right) \quad \text{and} \tag{D6}$$

$$\sigma^2 = \ln\left(1 + \frac{\sigma_\chi^2}{\mu_\chi^2}\right), \tag{D7}$$

where χ follows a normal distribution with mean (μ_χ) and variance (σ_χ^2) defined as

$$\mu_\chi = x_s / \overline{u} \quad \text{and} \tag{D8}$$

$$\sigma_\chi^2 = \frac{2D_{\text{eff}}\mu_\chi}{\overline{u}^2} = \frac{\langle|r_{\mu_\chi} - r_0|\rangle^2}{2\,\overline{u}^2}, \tag{D9}$$

where x_s is the x location of the sensor, $\overline{u}$ is the mean velocity, and $\langle|r_{\mu_\chi} - r_0|\rangle$ is the mean square particle pair separation at the mean travel time. Table II lists the resulting parameters at each sensor location, computed according to the equations above. Note that the lognormal distributions were also multiplied by a scaling factor ranging from 0.064 to 0.069, chosen such that the distributions have approximately the same peak value as the observed travel time probabilities. The scaling factor includes factors related to the ratio of power between correlated and independent components of the mapping function, which is beyond the scope of this study. The resulting lognormal distributions are the modeled a_0 single-particle travel time distributions, as plotted and compared with the actual distributions in Fig. 5 in the manuscript.

[1] G. Reddy, V. N. Murthy, and M. Vergassola, Olfactory Sensing and Navigation in Turbulent Environments, Annual Review of Condensed Matter Physics **13**, 191 (2022).

[2] B. Auffarth, Understanding smell—The olfactory stimulus problem, Neuroscience & Biobehavioral Reviews **37**, 1667 (2013).

[3] C.-Y. Su, K. Menuz, and J. R. Carlson, Olfactory Perception: Receptors, Cells, and Circuits, Cell **139**, 45 (2009).

[4] G. Laurent, M. Stopfer, R. W. Friedrich, M. I. Rabinovich, A. Volkovskii, and H. D. Abarbanel, Odor Encoding as an Active, Dynamical Process: Experiments, Computation, and Theory, Annual Review of Neuroscience **24**, 263 (2001).

[5] V. Jacob, C. Monsempès, J.-P. Rospars, J.-B. Masson, and P. Lucas, Olfactory coding in the turbulent realm, PLOS Computational Biology **13**, e1005870 (2017).

[6] P. Szyszka, R. C. Gerkin, C. G. Galizia, and B. H. Smith, High-speed odor transduction and pulse tracking by insect olfactory receptor neurons, Proceedings of the National Academy of Sciences **111**, 16925 (2014).

[7] A. Egea-Weiss, A. Renner, C. J. Kleineidam, and P. Szyszka, High Precision of Spike Timing across Olfactory Receptor Neurons Allows Rapid Odor Coding in Drosophila, iScience **4**, 76 (2018).

[8] A. Mafra-Neto and R. T. Cardé, Effect of the fine-scale structure of pheromone plumes: pulse frequency modulates activation and upwind flight of almond moth males, Physiological Entomology **20**, 229 (1995).

[9] A. Gumaste, K. L. Baker, M. Izydorczak, A. C. True, G. Vasan, J. P. Crimaldi, and J. Verhagen, Behavioral discrimination and olfactory bulb encoding of odor plume intermittency, eLife **13**, e85303 (2024).

[10] L. Conchou, P. Lucas, C. Meslin, M. Proffit, M. Staudt, and M. Renou, Insect Odorscapes: From Plant Volatiles to Natural Olfactory Scenes, Frontiers in Physiology **10**, 972 (2019).

[11] M. Pannunzi and T. Nowotny, Odor Stimuli: Not Just Chemical Identity, Frontiers in Physiology **10**, 1428 (2019).

[12] K. I. Nagel, E. J. Hong, and R. I. Wilson, Synaptic and circuit mechanisms promoting broadband transmission of olfactory stimulus dynamics, Nature Neuroscience **18**, 56 (2015).

[13] C. Martelli, J. R. Carlson, and T. Emonet, Intensity Invariant Dynamics and Odor-Specific Latencies in Olfactory Receptor Neuron Response, The Journal of Neuroscience **33**, 6285 (2013).

[14] T. Ackels, A. Erskine, D. Dasgupta, A. C. Marin, T. P. A. Warner, S. Tootoonian, I. Fukunaga, J. J. Harris, and A. T. Schaefer, Fast odour dynamics are encoded in the olfactory system and guide behaviour, Nature **593**, 558 (2021).

[15] H. Guo, K. Kunwar, and D. Smith, Odorant Receptor Sensitivity Modulation in *Drosophila*, The Journal of Neuroscience **37**, 9465 (2017).

[16] H. Guo and D. P. Smith, Time-Dependent Odorant Sensitivity Modulation in Insects, Insects **13**, 354 (2022).

[17] C.-Y. Su, C. Martelli, T. Emonet, and J. R. Carlson, Temporal coding of odor mixtures in an olfactory receptor neuron, Proceedings of the National Academy of Sciences **108**, 5075 (2011).

[18] D. Raccuglia, L. Y. McCurdy, M. Demir, S. Gorur-Shandilya, M. Kunst, T. Emonet, and M. N. Nitabach, Presynaptic GABA Receptors Mediate Temporal Contrast Enhancement in *Drosophila* Olfactory Sensory Neurons and Modulate Odor-Driven Behavioral Kinetics, eneuro **3**, ENEURO.0080 (2016).

[19] V. Jayaram, N. Kadakia, and T. Emonet, Sensing complementary temporal features of odor signals enhances navigation of diverse turbulent plumes, eLife **11**, e72415 (2022).

[20] N. Kadakia, M. Demir, B. T. Michaelis, B. D. DeAngelis, M. A. Reidenbach, D. A. Clark, and T. Emonet, Odour motion sensing enhances navigation of complex plumes, Nature **611**, 754 (2022).

[21] J. Murlis, Odor Plumes and the Signal They Provide, in *Insect Pheromone Research*, edited by R. T. Cardé and A. K. Minks (Springer US, Boston, MA, 1997) pp. 221–231.

[22] M. Wachowiak, A. Dewan, T. Bozza, T. F. O'Connell, and E. J. Hong, Recalibrating Olfactory Neuroscience to the Range of Naturally Occurring Odor Concentrations, The Journal of Neuroscience **45**, e1872242024 (2025).

[23] E. Villermaux, Mixing Versus Stirring, Annual Review of Fluid Mechanics **51**, 245 (2019).

[24] J. Murlis, M. A. Willis, and R. T. Cardé, Spatial and temporal structures of pheromone plumes in fields and forests, Physiological Entomology **25**, 211 (2000).

[25] A. Obukhov, On the Energy Distribution in the Spectrum of a Turbulent Flow, Doklady Akademii Nauk SSSR **32**, 22 (1941).

[26] A. Kolmogorov, The Local Structure of Turbulence in Incompressible Viscous Fluid for Very Large Reynolds' Numbers, Akademiia Nauk SSSR Doklady **30**, 301 (1941), aDS Bibcode: 1941DoSSR..30..301K.

[27] Z. Warhaft, Passive Scalars in Turbulent Flows, Annual Review of Fluid Mechanics **32**, 203 (2000).

[28] A. Celani, E. Villermaux, and M. Vergassola, Odor Landscapes in Turbulent Environments, Physical Review X **4**, 041015 (2014).

[29] S. Tootoonian, A. C. True, E. Stark, J. P. Crimaldi, and A. T. Schaefer, Quantifying spectral information about source separation in multisource odour plumes, PLOS ONE **20**, e0297754 (2025).

[30] C. Finelli, Velocity and concentration distributions in turbulent odor plumes in the presence of vegetation mimics: a flume study, Marine Ecology Progress Series **207**, 297 (2000).

[31] P. A. Moore and J. Atema, Spatial Information in the Three-Dimensional Fine Structure of an Aquatic Odor Plume, The Biological Bulletin **181**, 408 (1991).

[32] R. Shapley and P. Lennie, Spatial Frequency Analysis in the Visual System, (1985).

[33] S. L. Bressler and W. J. Freeman, Frequency analysis of olfactory system EEG in cat, rabbit, and rat, Electroencephalography and Clinical Neurophysiology **50**, 19 (1980).

[34] S. Shamma, On the role of space and time in auditory processing, Trends in Cognitive Sciences **5**, 340 (2001).

[35] A. Gescheider, S. Bolanowski, and K. Hardick, The fre-

quency selectivity of information-processing channels in the tactile sensory system, Somatosensory & Motor Research **18**, 191 (2001).
[36] K. I. Nagel and R. I. Wilson, Biophysical mechanisms underlying olfactory receptor neuron dynamics, Nature Neuroscience **14**, 208 (2011).
[37] A. J. Kim, A. A. Lazar, and Y. B. Slutskiy, System identification of Drosophila olfactory sensory neurons, Journal of Computational Neuroscience **30**, 143 (2011).
[38] See supplemental material at [url] for animations of three-dimensional plot rotations.
[39] S. P. Foster and K. G. Anderson, Sex pheromone biosynthesis, storage and release in a female moth: making a little go a long way, Proceedings of the Royal Society B: Biological Sciences **287**, 20202775 (2020).
[40] M. Rucci and J. D. Victor, The unsteady eye: an information-processing stage, not a bug, Trends in Neurosciences **38**, 195 (2015).
[41] X. Kuang, M. Poletti, J. Victor, and M. Rucci, Temporal Encoding of Spatial Information during Active Visual Fixation, Current Biology **22**, 510 (2012).
[42] M. Aytekin, J. D. Victor, and M. Rucci, The Visual Input to the Retina during Natural Head-Free Fixation, Journal of Neuroscience **34**, 12701 (2014).
[43] C. Nironi, P. Salizzoni, M. Marro, P. Mejean, N. Grosjean, and L. Soulhac, Dispersion of a Passive Scalar Fluctuating Plume in a Turbulent Boundary Layer. Part I: Velocity and Concentration Measurements, Boundary-Layer Meteorology **156**, 415 (2015).
[44] G. K. Batchelor, I. D. Howells, and A. A. Townsend, Small-scale variation of convected quantities like temperature in turbulent fluid Part 2. The case of large conductivity, Journal of Fluid Mechanics **5**, 134 (1959).
[45] L. Richardson, Atmospheric diffusion shown on a distance-neighbour graph, Proceedings of the Royal Society of London. Series A, Containing Papers of a Mathematical and Physical Character **110**, 709 (1926).
[46] M. Bourgoin, N. T. Ouellette, H. Xu, J. Berg, and E. Bodenschatz, The Role of Pair Dispersion in Turbulent Flow, Science **311**, 835 (2006).
[47] F. Nicolleau and G. Yu, Two-particle diffusion and locality assumption, Physics of Fluids **16**, 2309 (2004).
[48] D. R. Osborne, J. C. Vassilicos, K. Sung, and J. D. Haigh, Fundamentals of pair diffusion in kinematic simulations of turbulence, Physical Review E **74**, 036309 (2006).
[49] N. A. Malik, Turbulent particle pair diffusion: A theory based on local and non-local diffusional processes, PLOS ONE **13**, e0202940 (2018).
[50] P. K. Kundu, I. M. Cohen, P. S. Ayyaswamy, and H. H. Hu, *Fluid mechanics*, 4th ed. (Elsevier, London, 2007).
[51] S. B. Pope, *Turbulent flows* (Cambridge University Press, Cambridge ; New York, 2000).
[52] B. K. Martin, X. L. Wu, W. I. Goldburg, and M. A. Rutgers, Spectra of Decaying Turbulence in a Soap Film, Physical Review Letters **80**, 3964 (1998).
[53] S. Gorur-Shandilya, M. Demir, J. Long, D. A. Clark, and T. Emonet, Olfactory receptor neurons use gain control and complementary kinetics to encode intermittent odorant stimuli, eLife **6**, e27670 (2017).
[54] M. Levakova, L. Kostal, C. Monsempès, V. Jacob, and P. Lucas, Moth olfactory receptor neurons adjust their encoding efficiency to temporal statistics of pheromone fluctuations, PLOS Computational Biology **14**, e1006586 (2018).
[55] A. Nag and F. Van Breugel, Odour source distance is predictable from a time history of odour statistics for large scale outdoor plumes, Journal of The Royal Society Interface **21**, 20240169 (2024).
[56] M. Schmuker, V. Bahr, and R. Huerta, Exploiting plume structure to decode gas source distance using metal-oxide gas sensors, Sensors and Actuators B: Chemical **235**, 636 (2016).
[57] L. Biferale, G. Boffetta, A. Celani, B. J. Devenish, A. Lanotte, and F. Toschi, Lagrangian statistics of particle pairs in homogeneous isotropic turbulence, Physics of Fluids **17**, 115101 (2005).
[58] R. Shnapp, S. Brizzolara, M. M. Neamtu-Halic, A. Gambino, and M. Holzner, Universal alignment in turbulent pair dispersion, Nature Communications **14**, 4195 (2023).
[59] P. Szyszka, T. Emonet, and T. L. Edwards, Extracting spatial information from temporal odor patterns: insights from insects, Current Opinion in Insect Science **59**, 101082 (2023).
[60] B. T. Michaelis, K. W. Leathers, Y. V. Bobkov, B. W. Ache, J. C. Principe, R. Baharloo, I. M. Park, and M. A. Reidenbach, Odor tracking in aquatic organisms: the importance of temporal and spatial intermittency of the turbulent plume, Scientific Reports **10**, 7961 (2020).
[61] J. I. Raji, J. K. Konopka, and C. J. Potter, A spatial map of antennal-expressed ionotropic receptors in the malaria mosquito, Cell Reports **42**, 112101 (2023).
[62] L. B. Vosshall, H. Amrein, P. S. Morozov, A. Rzhetsky, and R. Axel, A Spatial Map of Olfactory Receptor Expression in the Drosophila Antenna, Cell **96**, 725 (1999).
[63] C. Chen, C. Kachramanoglou, D. Li, P. Andrews, and D. Choi, Anatomy and Cellular Constituents of the Human Olfactory Mucosa: A Review, Journal of Neurological Surgery Part B: Skull Base **75**, 293 (2014).
[64] B. Zapiec and P. Mombaerts, The Zonal Organization of Odorant Receptor Gene Choice in the Main Olfactory Epithelium of the Mouse, Cell Reports **30**, 4220 (2020).
[65] J. Murlis, J. S. Elkinton, and R. T. Cardé, Odor Plumes and How Insects Use Them, Annual Review of Entomology **37**, 505 (1992).
[66] T. A. Keller and M. J. Weissburg, Effects of Odor Flux and Pulse Rate on Chemosensory Tracking in Turbulent Odor Plumes by the Blue Crab, *Callinectes sapidus*, The Biological Bulletin **207**, 44 (2004).
[67] H. Kim, G. Lee, J. Song, and S.-G. Kim, Real-Time Visualization of Scent Accumulation Reveals the Frequency of Floral Scent Emissions, Frontiers in Plant Science **13**, 835305 (2022).
[68] L. Kang, J. Kaur, K. Winkeler, D. Kubiak, and J. E. Hill, How the volatile organic compounds emitted by corpse plant change through flowering, Scientific Reports **13**, 372 (2023).
[69] H. Tichy, A. Hinterwirth, and E. Gingl, Olfactory receptors on the cockroach antenna signal odour ON and odour OFF by excitation, European Journal of Neuroscience **22**, 3147 (2005).
[70] M. Vergassola, E. Villermaux, and B. I. Shraiman, 'Infotaxis' as a strategy for searching without gradients, Nature **445**, 406 (2007).
[71] S. D. Boie, E. G. Connor, M. McHugh, K. I. Nagel, G. B. Ermentrout, J. P. Crimaldi, and J. D. Victor, Information-theoretic analysis of realistic odor plumes:

What cues are useful for determining location?, PLOS Computational Biology **14**, e1006275 (2018).
[72] A. Sunil, O. Pedroncini, A. T. Schaefer, and T. Ackels, How do mammals convert dynamic odor information into neural maps for landscape navigation?, PLOS Biology **22**, e3002908 (2024).
[73] J. Crimaldi, H. Lei, A. Schaefer, M. Schmuker, B. H. Smith, A. C. True, J. V. Verhagen, and J. D. Victor, Active sensing in a dynamic olfactory world, Journal of Computational Neuroscience **50**, 1 (2022).
[74] M. Wachowiak, All in a Sniff: Olfaction as a Model for Active Sensing, Neuron **71**, 962 (2011).
[75] F. Gascue, E. Marachlian, M. Azcueta, F. F. Locatelli, and M. Klappenbach, Antennal movements can be used as behavioral readout of odor valence in honey bees, IBRO Neuroscience Reports **12**, 323 (2022).
[76] S. Tripathy, Odors pulsed at wing beat frequencies are tracked by primary olfactory networks and enhance odor detection, Frontiers in Cellular Neuroscience 10.3389/neuro.03.001.2010 (2010).
[77] R. R. Anholt, Molecular physiology of olfaction, American Journal of Physiology-Cell Physiology **257**, C1043 (1989).
[78] E. A. Corey and B. W. Ache, Comparative Olfactory Transduction, in *Chemosensory Transduction* (Elsevier, 2016) pp. 207–223.
[79] G. T. Csanady, Concentration Fluctuations in Turbulent Diffusion, Journal of the Atmospheric Sciences **24**, 21 (1967).
[80] A. A. Townsend, *The structure of turbulent shear flow*, 2nd ed., Cambridge monographs on mechanics and applied mathematics (Cambridge university press, Cambridge [GB] New York New Rochelle, 1980).
[81] P. A. Durbin, A stochastic model of two-particle dispersion and concentration fluctuations in homogeneous turbulence, Journal of Fluid Mechanics **100**, 279 (1980).
[82] B. Sawford, Turbulent relative dispersion, Annual Review of Fluid Mechanics **33**, 289 (2001).
[83] M. Cassiani, M. B. Bertagni, M. Marro, and P. Salizzoni, Concentration Fluctuations from Localized Atmospheric Releases, Boundary-Layer Meteorology **177**, 461 (2020).
[84] D. J. Thomson, A stochastic model for the motion of particle pairs in isotropic high-Reynolds-number turbulence, and its application to the problem of concentration variance, Journal of Fluid Mechanics **210**, 113 (1990).
[85] P. K. Yeung, Direct numerical simulation of two-particle relative diffusion in isotropic turbulence, Physics of Fluids **6**, 3416 (1994).
[86] A. Arnèodo, R. Benzi, J. Berg, L. Biferale, E. Bodenschatz, A. Busse, E. Calzavarini, B. Castaing, M. Cencini, L. Chevillard, R. Fisher, R. Grauer, H. Homann, D. Lamb, A. S. Lanotte, E. Lévèque, B. Lüthi, J. Mann, N. Mordant, W.-C. Müller, S. Ott, N. T. Ouellette, J.-F. Pinton, S. B. Pope, S. G. Roux, F. Toschi, H. Xu, and P. K. Yeung, Universal Intermittent Properties of Particle Trajectories in Highly Turbulent Flows, Physical Review Letters **100**, 254504 (2008).
[87] D. J. Thomson, Eulerian analysis of concentration fluctuations in dispersing plumes and puffs, Physics of Fluids **9**, 2349 (1997).
[88] M. Cassiani, P. Franzese, and U. Giostra, A PDF micromixing model of dispersion for atmospheric flow. Part I: development of the model, application to homogeneous turbulence and to neutral boundary layer, Atmospheric Environment **39**, 1457 (2005).
[89] R. Benzi and A. Vulpiani, Multifractal approach to fully developed turbulence, Rendiconti Lincei. Scienze Fisiche e Naturali **33**, 471 (2022).
[90] J. E. Fackrell and A. G. Robins, The effects of source size on concentration fluctuations in plumes, Boundary-Layer Meteorology **22**, 335 (1982).
[91] R. I. Sykes, W. S. Lewellen, and S. F. Parker, A turbulent-transport model for concentration fluctuations and fluxes, Journal of Fluid Mechanics **139**, 193 (1984).
[92] N. Rigolli, G. Reddy, A. Seminara, and M. Vergassola, Alternation emerges as a multi-modal strategy for turbulent odor navigation, eLife **11**, e76989 (2022).
[93] S. Gorur-Shandilya, C. Martelli, M. Demir, and T. Emonet, Controlling and measuring dynamic odorant stimuli in the laboratory, Journal of Experimental Biology , jeb.207787 (2019).
[94] E. Stark, J. Crimaldi, A. True, and J. D. Victor, Temporal reformatting of odor signals by flow environments: CFD dataset (2025).
[95] Z. Zhou, L. Fang, N. T. Ouellette, and H. Xu, Vorticity gradient stretching in the direct enstrophy transfer process of two-dimensional turbulence, Physical Review Fluids **5**, 054602 (2020).
[96] J. P. Crimaldi and J. R. Koseff, High-resolution measurements of the spatial and temporal scalar structure of a turbulent plume, Experiments in Fluids **31**, 90 (2001).
[97] H. Lim and C. Vanderwel, Turbulent dispersion of a passive scalar in a smooth-wall turbulent boundary layer, Journal of Fluid Mechanics **969**, A26 (2023).
[98] J. J. Hopfield, Olfactory computation and object perception., Proceedings of the National Academy of Sciences **88**, 6462 (1991).
[99] A. Sehdev and P. Szyszka, Segregation of Unknown Odors From Mixtures Based on Stimulus Onset Asynchrony in Honey Bees, Frontiers in Behavioral Neuroscience **13**, 155 (2019).
[100] A. Sehdev, Y. G. Mohammed, T. Triphan, and P. Szyszka, Olfactory Object Recognition Based on Fine-Scale Stimulus Timing in Drosophila, iScience **13**, 113 (2019).
[101] O. Schenk, K. Gärtner, W. Fichtner, and A. Stricker, PARDISO: a high-performance serial and parallel sparse linear solver in semiconductor device simulation, Future Generation Computer Systems **18**, 69 (2001).
[102] M. Klein, Integral Turbulent Length and Time Scales of Higher Order Moments, Flow, Turbulence and Combustion **112**, 397 (2024).
[103] J. P. Salazar and L. R. Collins, Two-Particle Dispersion in Isotropic Turbulent Flows, Annual Review of Fluid Mechanics **41**, 405 (2009).
[104] E. Yee, P. R. Kosteniuk, G. M. Chandler, C. A. Biltoft, and J. F. Bowers, Statistical characteristics of concentration fluctuations in dispersing plumes in the atmospheric surface layer, Boundary-Layer Meteorology **65**, 69 (1993).
[105] P. L. Miller and P. E. Dimotakis, Measurements of scalar power spectra in high Schmidt number turbulent jets, Journal of Fluid Mechanics **308**, 129 (1996).
[106] M. Mohaghar, L. P. Dasi, and D. R. Webster, Scalar power spectra and turbulent scalar length scales of

high-Schmidt-number passive scalar fields in turbulent boundary layers, Physical Review Fluids **5**, 084606 (2020).